Research Square

Preprints are preliminary reports that have not undergone peer review.
They should not be considered conclusive, used to inform clinical practice,
or referenced by the media as validated information.

Borehole stress profiling from inversion of injection-induced fracture displacements

Kai Bröker

kai.broeker@unine.ch

University of Neuchâtel

Yves Guglielmi

Lawrence Berkeley National Laboratory

Florian Soom

Lawrence Berkeley National Laboratory

Paul Cook

Lawrence Berkeley National Laboratory

Marian Hertrich

ETH Zurich

Benoît Valley

University of Neuchâtel

Research Article

Keywords: Fracture slip, Stress inversion, Underground research laboratory, Fractured crystalline rock, Bedretto Underground Laboratory for Geosciences and Geoenergies

Posted Date: November 19th, 2026

DOI: https://doi.org/10.21203/rs.3.rs-11484543/v1

License: This work is licensed under a Creative Commons Attribution 4.0 International License.
Read Full License

Additional Declarations: No competing interests reported.

Borehole stress profiling from inversion of injection-induced fracture displacements

Kai Bröker[1,*], Yves Guglielmi[2], Florian Soom[2], Paul Cook[2], Marian Hertrich[3], and Benoît Valley[1]

[1] *Center for Hydrogeology and Geothermics, University of Neuchâtel, Neuchâtel, Switzerland*
[2] *Lawrence Berkeley National Laboratory, Energy Geoscience Division, USA*
[3] *Department of Earth and Planetary Sciences, ETH Zürich, Zürich, Switzerland*
[*] *Corresponding author: Kai Bröker (kai.broeker@unine.ch)*

October 23, 2026

Abstract

Knowledge of the in situ stress field and its spatial heterogeneity is essential for the safe development of the subsurface, yet most borehole-based methods resolve only part of the stress tensor or make simplifying assumptions. This study presents an improved inversion method to estimate the full stress tensor from three-dimensional fracture displacement data measured in a borehole interval during fluid injection. By combining three-dimensional displacement measurements with pressure transient analysis, the method enables stress tensor estimation from a single test. We conducted 11 injection tests and applied the method to nine test intervals along a 61 m long section of an inclined borehole at the Bedretto Underground Laboratory for Geosciences and Geoenergies (BedrettoLab), Switzerland, with an overburden of more than 1100 m. The inversion constrains the orientation of the least principal stress (S_3) considerably better than those of the greatest (S_1) and intermediate (S_2) principal stresses, which are distributed along a girdle normal to S_3 and can interchange their orientations. All inverted intervals indicate a normal faulting regime with S_3 magnitudes of 8.5–15.1 MPa and S_1 inclined by 15°–37° from the vertical direction. Away from the fault zone, S_3 is consistent with the far-field N22°E orientation, independently determined by hydraulic fracturing stress measurements. Close to a large fault zone intersected by the borehole, S_3 rotates counterclockwise by up to 68°, while the stress magnitudes vary little. The stress rotation is asymmetric and decays within 4–8 m above the fault zone but persists over 17–23 m below it, in agreement with the wider fractured zone below the fault core. Our results demonstrate that the stress inversion can resolve meter-scale stress heterogeneity around a fault zone without the need for multiple tests or assumptions on the principal stress orientations, which is relevant for the design of hydraulic stimulation and fault reactivation experiments.

Keywords: Fracture slip, Stress inversion, Underground research laboratory, Fractured crystalline rock, Bedretto Underground Laboratory for Geosciences and Geoenergies

1 Introduction

Accurately measuring in situ stress is critical for the safe and effective development of the subsurface. Stress measurements and stress profiling are fundamental to predicting how subsurface features will respond to engineering interventions such as fluid injections or underground construction processes (e.g., Amadei and Stephansson, 1997; Zoback, 2007; Zang and Stephansson, 2010; Doonechaly et al., 2025). In projects such as nuclear waste disposal, CO_2 storage, and enhanced geothermal systems (EGS) at depths of typically 1–5 km, the local stress field is influenced by complex geological features, including natural fractures and fault zones (e.g., Valley and Evans, 2010; Chang and Jo, 2015; Krietsch et al., 2019; Zhang et al., 2023), as well as varying rock properties (e.g., Ma and Zoback, 2017; Ma et al., 2022b; Talukdar et al., 2022). As a result, the local stress state may deviate from the regional stress field, whose orientation of the maximum horizontal stress (S_{Hmax}) is often assumed to be relatively uniform over large regions. Indeed, various studies have shown that the local stress state exhibits spatial heterogeneity at different scales, ranging from a few meters to hundreds of meters (e.g., Shamir and Zoback, 1992; Valley and Evans, 2009, 2010; Day-Lewis et al., 2010; Zhang et al., 2023). At the smaller end of this scale, meter-scale stress perturbations have been observed in boreholes and are often associated with geological structures such as faults and fractures (Barton and Zoback, 1994; Sahara et al., 2014; Chang and Jo, 2015; Krietsch et al., 2019; Zhang et al., 2023). Such heterogeneity poses a challenge for stress characterization, as point measurements alone cannot determine whether the recorded values are affected by local disturbances or representative of the stress field at the site scale. For this reason, distributed measurements along a profile are required to robustly characterize the stress field at a site.

A variety of techniques are currently available for estimating in situ rock stress (Amadei and Stephansson, 1997; Ljunggren et al., 2003). The selection of a particular method is dependent on the scale of the rock volume under investigation, as well as the accessibility of the subsurface and logistical constraints. In deep boreholes, the most commonly adopted methods are borehole-based hydraulic techniques. Two classical hydraulic approaches are generally employed (Haimson and Cornet, 2003): (1) the conventional hydraulic fracturing (HF), which involves creating new fractures, and (2) the hydraulic testing of pre-existing fractures (HTPF), which reactivates natural fractures. The HF method reliably constrains the magnitude and orientation of the least principal stress (S_3). Under the assumption of a vertical borehole and a stress regime in which two of the principal stresses are horizontal, and with additional simplifying assumptions, the magnitude and orientation of S_{Hmax} can also be inferred (Bröker and Ma, 2022). Alternatively, HF can be combined with the analysis of compressional (breakouts) and tensile (drilling-induced tensile fractures) borehole failures, if present (Brudy et al., 1997). HTPF tests can be used to determine the complete 3D stress tensor, but a minimum of six to eight tests conducted on fractures with sufficiently different orientations are needed. Moreover, the stress field must be assumed to vary linearly across these

tests, which becomes increasingly limiting as the spacing between test locations increases.

This paper presents an extension of an existing inverse method to determine the complete 3D stress tensor based on fracture displacement measured during fluid injection in a borehole (Kakurina, 2019; Kakurina et al., 2020; Guglielmi et al., 2021b). The method finds stress tensors that are consistent with the estimated fracture activation vector, which describes the fracture displacement that occurs once fluid pressure is sufficiently high to induce fracture reactivation. The number of solutions is further reduced by taking into account the measured pressure and flow rate record during injection, as well as the estimated overburden stress at the test location. The inverted stress tensors are analyzed using the Euclidean mean stress tensor to capture their tensorial characteristics. To facilitate interpretation, we illustrate and discuss the three principal stress magnitudes and orientations and their uncertainties.

Fracture displacement is measured with the three-component borehole deformation tool (SIMFIP = step-rate injection method for fracture in situ properties) presented in Guglielmi et al. (2014). The SIMFIP probe is a double-packer probe instrumented with a high-resolution fiber-optic 3D displacement sensor and a fluid pressure sensor inside the injection interval. This probe has been deployed in various settings including clay rocks at the Mont-Terri laboratory (Kakurina et al., 2020), limestones at the Low-Noise Underground Laboratory (LSBB) (Duboeuf et al., 2021; Cappa et al., 2022), metamorphic rocks at the Sanford Underground Research Facility (SURF) (Guglielmi et al., 2023), and crystalline rocks in the Collisional Orogeny in the Scandinavian Caledonides (COSC) scientific drilling project (Guglielmi et al., 2025). More recently, the SIMFIP tool has been deployed at the Bedretto Underground Laboratory for Geosciences and Geoenergies (BedrettoLab; Ma et al. 2022a) in the framework of the SPINE (Stress Profiling In EGS) project (Bröker et al., 2025, 2026). The goal of the project is to advance stress profiling techniques in crystalline rock for safer and more efficient deep geothermal energy development. A total of 11 tests were conducted along an inclined borehole at the BedrettoLab Earthquake Physics testbed (Meier et al., 2026). The tests span a length of around 61 m and target either one or multiple pre-existing fractures, intact rock sections, or a large fault zone intersected by the borehole. We present the results of the complete stress profile and show that the intersected fault zone leads to a stress perturbation that mainly affects the stress orientation.

2 Site description

2.1 Bedretto Underground Laboratory

The Bedretto Underground Laboratory for Geosciences and Geoenergies (BedrettoLab) is a research facility operated by ETH Zurich since 2018. The BedrettoLab is located in the 5.2 km long Bedretto

Tunnel (Ticino, Switzerland; Fig. 1), which is an auxiliary access drift of the Furka Base Tunnel. Large parts of the Bedretto Tunnel are unlined and have a width and height of about 3 m. Several testbeds exist within the BedrettoLab, whereby we focus on experiments conducted in the Earthquake Physics testbed. This testbed is located around 2.3 km from the tunnel entrance, and it consists of several exploration and monitoring boreholes. The testbed is dedicated to advancing the fundamental understanding of earthquake physics, and multiple stimulation experiments in the so-called MC fault zone are currently ongoing (Achtziger-Zupančič et al., 2024; Meier et al., 2026).

The Earthquake Physics testbed and most of the Bedretto Tunnel are located within the Rotondo granite, which is relatively homogeneous, massive, light gray and shows only minor influence of metamorphism (Lützenkirchen and Loew, 2011; Rast et al., 2022; Ceccato et al., 2024). The topography above the Bedretto Tunnel varies considerably and the overburden is about 1135 m at the location of the Earthquake Physics testbed. Fracture zones and faults along the Bedretto Tunnel dip steeply to subvertically (>60°), with a notable absence of structures dipping between east and south (Bröker et al., 2024). The dominant strike of the major structures (fault zones) ranges from NE–SW (tunnel-perpendicular) to E–W. Additional sets strike N–S and NW–SE (tunnel-parallel).

The MC fault zone, which intersects the borehole investigated in this study, is part of this dominant set of NE–SW to E–W striking structures and dips steeply towards the NW. It belongs to the youngest, brittle generation of structures in the Rotondo granite, which is characterized by zeolite- and gouge-bearing shear surfaces that reactivated older ductile shear zones (Ceccato et al., 2024), and it has an expected lateral extent of more than 100 m (Achtziger-Zupančič et al., 2024). Having developed on a pre-existing zone of high fracture intensity, the MC fault is considered an immature fault zone, with a weakly developed damage zone and no evidence of a continuous low-permeability fault core (Achtziger-Zupančič et al., 2024; Schaber et al., 2026).

2.2 Previous stress measurements

Extensive stress characterization was conducted at the BedrettoLab using small hydraulic fracturing tests, often referred to as mini-frac tests. These tests were conducted in the vicinity of the geothermal testbed in six 30–40 m long stress measurement boreholes (Bröker and Ma, 2022; Bröker et al., 2024). The closest of these boreholes is approximately 100 m from the borehole analyzed in this study, whereas the geothermal testbed itself is located approximately 300 m away. Additional mini-frac tests were conducted in several boreholes of the Earthquake Physics testbed. Their results are presented in Kövér et al. (2026) and compared with our results in Section 5.2.

Overall, the stress state at the BedrettoLab is transitional between normal and strike-slip faulting ($S_{\mathrm{hmin}} < S_{\mathrm{Hmax}} \leq S_v$, where S_{hmin} = minimum horizontal stress, S_{Hmax} = maximum horizontal stress,

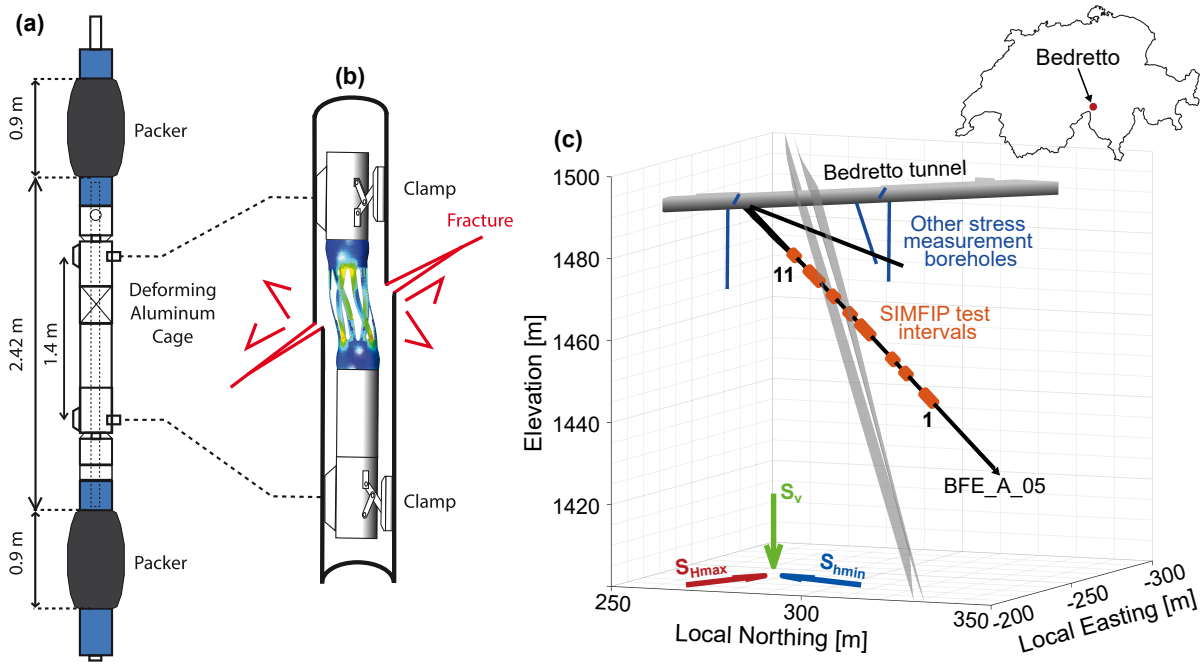


Figure 1: a) Schematic of the SIMFIP probe. b) Detailed view of the deformation cage. c) Location of the SIMFIP test intervals in the Earthquake Physics testbed at the BedrettoLab. Note that the full length of borehole BFE_A_05 is not shown. Far-field stress orientations are taken from Bröker et al. (2024). Figure modified after Bröker et al. (2026).

S_v = vertical stress). The average stress magnitudes around the geothermal testbed are (Bröker and Ma, 2022): $S_{\mathrm{hmin}} = 14.6 \pm 1.4$ MPa, $S_{\mathrm{Hmax}} = 25.4 \pm 2.3$ MPa, $S_v \approx 26.5$ MPa. According to the hydraulic fracture azimuth derived from acoustic televiewer (ATV) logs, the average far-field S_{Hmax} orientation is estimated to be N112°E (Bröker et al., 2024). In addition, the vertical direction is approximately a principal stress direction (S_v), although a small inclination (<10°) is possible. Observations of borehole breakout rotations (Zhang et al., 2023) and hydraulic fracture trace variability (Bröker et al., 2024) indicate that local stress field variations exist, mainly due to stress perturbation and reorientation effects around natural fractures and fault zones. The local pore pressure in the geothermal testbed ranges from 2.0 to 5.6 MPa and is below hydrostatic values due to tunnel drainage and pressure drawdown (Bröker and Ma, 2022), whereas in the Earthquake Physics testbed, Schaber et al. (2026) measured static pore pressures of 0.7 to 3.6 MPa across the MC fault zone in BFE_A_05.

2.3 Stress profiling along borehole BFE_A_05

This study examines 11 SIMFIP test intervals along borehole BFE_A_05 at the BedrettoLab (Fig. 1c). The tests were conducted in December 2022. Borehole BFE_A_05 was core-drilled to a length of 216 m with a diameter of 96 mm, and it dips on average 30.2° towards the northeast (N30.9°E). The borehole trajectory based on ATV logging data is shown in Appendix A. Table 1 lists the locations of the 11 test intervals, which span approximately 61 m along the upper part of the borehole. Test locations were

selected using borehole logs and cores, to optimally represent intervals with intact rock and intervals with pre-existing fractures. The tests targeted either one or multiple pre-existing fractures, intact rock sections, or a large fault zone intersecting the borehole.

The borehole BFE_A_05 intersects the MC fault zone, which was characterized in detail by Schaber et al. (2026) based on petrophysical analysis of core samples, geophysical logs, and single- and cross-hole hydraulic tests. Based on the core facies classification of Achtziger-Zupančič et al. (2024), Schaber et al. (2026) delineated the MC fault zone in BFE_A_05 between 35.0 and 47.0 m MD, where sealed and non-cohesive fractures, increased matrix porosity, and a mylonitic to cataclastic fabric replace the intact host granite. The fault core, defined here as the section of intensely fractured rock with fine gouge or cataclastic breccia, is confined to 37.5–39.0 m MD (Schaber et al., 2026).

Table 1: Specifications of the SIMFIP test intervals along borehole BFE_A_05. Depths refer to the interval midpoints. MD = measured depth, TVD = true vertical depth below the borehole collar

Test	Depth		Injected Volume [L]	Test target
	[m MD]	[m TVD]		
1	81.6	41.0	250	Pre-existing fracture
2	79.2	39.7	172	Pre-existing fracture
3	70.2	35.1	277	Pre-existing fracture
4	64.3	32.1	151	Pre-existing fracture
5	53.5	26.6	170	Intact rock
6	50.4	25.0	135	Multiple pre-existing fractures
7	45.2	22.4	410	Ductile shear zone, multiple pre-existing fractures
8	37.8	18.7	1526	Brittle fault zone with gouge, multiple pre-existing fractures
9	30.9	15.3	101	Multiple pre-existing fractures
10	27.5	13.6	150	Intact rock
11	20.3	10.0	109	Intact rock

3 Methodology

3.1 SIMFIP probe

The injection tests were conducted using a 6 m long SIMFIP probe (Fig. 1a; Guglielmi et al. 2014). The probe consists of a high-pressure double-packer system, a deformation cage equipped with seven Fiber Bragg Grating (FBG) strain sensors (Fig. 1b), and a hydraulic clamping mechanism that anchors the deformation cage to the borehole wall. The 2.42 m long injection interval was isolated by two 0.9 m long packers, with the SIMFIP clamps positioned 0.7 m above and below the center of the interval. The deformation cage within the injection interval is designed to measure the relative three-dimensional (3D) displacement between the upper and lower anchors. The cage consists of six uniaxial FBG strain sensors, which are mechanically clamped to the six deformable wings of the cage. Each FBG sensor measures strain

along a single direction. Together, the six sensors enable the continuous monitoring of cage deformation in six independent uniaxial directions at a sampling rate of 40 Hz. In addition, a seventh, unstressed FBG sensor is included to correct the measurements for ambient pressure and temperature effects.

When fluid pressure increases within the sealed interval and a fracture is initiated or reactivated, the SIMFIP system records the displacement of the upper clamp relative to the lower clamp (Fig. 1b). The axial and radial displacement ranges are ± 0.7 mm and ± 3.5 mm, respectively, and the corresponding resolutions are 0.1 μm. A compass allows orientation of the 3D measurements in magnetic or geographic coordinates. Note that the displacement sensor also measures the rotations around the three orthogonal axes with a range of 0.04 radians and a resolution of 0.1 μradians. Throughout the tests, a Micron Optics si155 fiber-optic interrogator continuously recorded all FBG strain measurements at the surface. Flow rate and pressures (interval and packer) were also measured at the surface (uphole) using a flowboard. A pump with a maximum flow rate of 10 L/min was used for injection.

3.2 Injection protocols and activation vector estimation

Once the probe was positioned within a test interval and the packers and clamps were set, a modified HTPF injection protocol was carried out. Each test began with a series of constant flow rate fracturing cycles aimed at initiating new fractures or stimulating pre-existing ones. This was followed by a step-rate test consisting of step-up and step-down sequences to determine the fracture reopening (also termed jacking) pressure, used as a proxy for the normal stress acting on the fracture. The key idea of the step-rate tests is to bring the fracture to slip progressively by decreasing the effective normal stress clamping the fracture step by step. All injections were conducted flow rate-controlled.

To simplify the interpretation of the complex 3D displacement data, we estimated incremental changes in displacement at each flow rate step (incremental displacement vectors), obtaining a complete set of displacement directions and magnitudes for each change in applied flow and pressure. We then retained only the steps for which pressure, flow, and tool movement indicate the onset of non-elastic rock displacement, signifying the activation of a new or pre-existing fracture. The displacement vectors of these retained steps are hereafter referred to as incremental activation vectors. We restrict the incremental activation vectors to this early phase of reactivation and exclude the displacement accumulated during subsequent fracture propagation, because continued slip and rupture growth progressively perturb the local stress field that the inversion aims to recover. Moreover, a heterogeneous fluid-pressure distribution along the fracture can alter the local shear stress orientation along the fracture, especially when dilation and aperture variations are significant (Kakurina et al., 2019). For each interval, we summed the retained incremental activation vectors to obtain the activation vector, which is assumed to represent the total

slip and opening during fracture activation. Its direction thus corresponds to the mean of the individual activation directions, weighted by their displacement magnitudes. All vectors were corrected for the clamp location, so that they describe the movement of the hanging wall relative to the footwall. These activation vectors were used as input for the stress tensor inversion.

The residual displacement vector at the end of each test was also evaluated. In some intervals, experimental artifacts, specifically probe unclamping during test 1, optical fiber failure during test 3, and cases where the fracture was located outside the deformation cage (tests 5, 10, and 11), introduce significant uncertainty in the residual vector orientation and likely lead to an underestimation of the residual displacement magnitude. However, because displacement magnitudes are not considered in the stress tensor inversion, the residual displacement vectors are not discussed further in this paper. A detailed presentation of these vectors is provided in Soom et al. (2026).

3.3 Inversion of fracture slip (SIMFIPinv)

SIMFIPinv is a code developed to estimate the full stress tensor from measured slip vectors on fracture planes. The underlying methodology is described in Kakurina (2019); Kakurina et al. (2020); Bröker et al. (2025) and summarized below. The code was further refined during the analysis presented in this work. The inversion is based on the Wallace–Bott hypothesis, which states that fracture slip occurs in the direction of the maximum resolved shear stress on the fracture plane (Wallace, 1951; Bott, 1959). Additional assumptions are that the fracture normal stress and the vertical stress at the test depth can be independently estimated, and that the orientation of the reactivated or created fracture is known.

The stress inversion is carried out within a predefined search space of candidate stress tensors. Following Yamaji (2003), we use a computational grid of 59400 reduced stress tensors. The grid consists of 300 directions of S_3 with nearly uniform spacing (Fig. 2), 18 directions of S_1 for each S_3 direction with a spacing of 10°, and 11 variations of the stress ratio ϕ, sampled at 0.1 intervals between 0 and 1 for each combination of S_1 and S_3. Each grid point is a reduced stress tensor that consists of four parameters: three Euler angles, which represent the stress orientations, and the stress ratio ϕ (Angelier, 1979), which characterizes the relative stress magnitudes and is defined as

$$\phi = \frac{S_2 - S_3}{S_1 - S_3}, \tag{1}$$

where S_1 is the greatest principal stress, S_2 is the intermediate principal stress, and S_3 is the least principal stress.

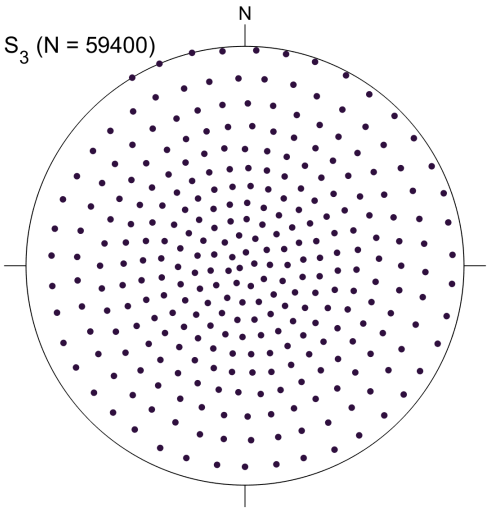


Figure 2: Lower-hemisphere equal-angle stereonet of 300 S_3-axis directions of the computational grid after Yamaji (2003). The angular distance between neighboring S_3 directions is not uniform, with a mean of 8.3° ± 1°. For each S_3 direction, there are 18 S_1 directions with 11 different stress ratios ϕ each, resulting in a total of 59400 stress tensors.

To reduce the large grid of reduced stress tensors, we perform a first solution reduction step based on the measured activation vector. For each reduced stress tensor in our computational grid, we compute the expected slip direction of the fracture identified in the test interval. Here, we assume that the shear displacement of a fracture can be modeled according to the Wallace–Bott hypothesis (Wallace, 1951; Bott, 1959). We then calculate the misfit angle between the predicted slip direction and the measured slip direction, i.e., the activation vector projected onto the fracture plane (projected activation vector), and keep only tensors with a misfit angle of 5° or less.

In the second solution reduction step, we calculate the principal stress magnitudes S_1, S_2, and S_3 by considering the estimations of the fracture normal stress S_n and vertical stress S_v at the test interval depth. The vertical stress is estimated by integrating the overburden at the test depth (Appendix B), and the fracture normal stress is estimated by pressure transient analysis (Appendix C). For each reduced stress tensor, we solve the system of equations in Eqs. (1)–(3). Here, l_1, m_1, n_1 are the direction cosines of the fracture normal, and l_2, m_2, n_2 are those of the vertical direction, both with respect to the principal stress axes.

$$S_n = l_1^2 S_1 + m_1^2 S_2 + n_1^2 S_3 \tag{2}$$

$$S_v = l_2^2 S_1 + m_2^2 S_2 + n_2^2 S_3 \tag{3}$$

After computing the principal stress magnitudes, we discard all solutions that fall outside the physically meaningful range. Specifically, we eliminate those with $S_3 < 3$ MPa or $S_1 > 50$ MPa. We also discard all solutions that do not satisfy the required principal stress ordering $S_1 \geq S_2 \geq S_3$. Together, these two reduction steps result in a range of physically admissible stress tensors consistent with the

measured activation vector and the independently estimated stress constraints (S_n and S_v).

3.4 Calculation of the mean stress tensor and visualization

We visualize and statistically analyze all admissible stress tensors for each interval to assess the variability and robustness of the inversion results. Additionally, we calculate the mean stress tensor as the Euclidean mean of all admissible stress tensors (Gao and Harrison, 2019), providing a representative stress state for further interpretation and comparison across test intervals. Given N stress tensors $\mathbf{S}_i$, the Euclidean mean stress tensor $\bar{\mathbf{S}}$ is defined as:

$$\bar{\mathbf{S}} = \frac{1}{N}\sum_{i=1}^{N}\mathbf{S}_i = \begin{bmatrix} \bar{S}_{xx} & \bar{\tau}_{xy} & \bar{\tau}_{xz} \\ & \bar{S}_{yy} & \bar{\tau}_{yz} \\ \text{symmetric} & & \bar{S}_{zz} \end{bmatrix} = \frac{1}{N}\begin{bmatrix} \sum_{i=1}^{N} S_{x_i} & \sum_{i=1}^{N} \tau_{xy_i} & \sum_{i=1}^{N} \tau_{xz_i} \\ & \sum_{i=1}^{N} S_{y_i} & \sum_{i=1}^{N} \tau_{yz_i} \\ \text{symmetric} & & \sum_{i=1}^{N} S_{z_i} \end{bmatrix}. \tag{4}$$

This approach preserves the tensorial nature of stress, providing physically reasonable results, such as orthogonally oriented principal stress axes, and a unique mean stress tensor for each interval.

To visualize the spread of orientations across all admissible stress tensors, we computed contour lines representing the density of the principal stress axes in a stereographic projection using the modified Kamb method with exponential smoothing (Kamb, 1959; Vollmer, 1995). The smoothing is scaled with the number of data points N such that it corresponds to a Kamb counting area for which the expected count E of a uniform (random) distribution equals three standard deviations ($E = 3\sigma$). Densities are expressed in multiples of uniform density (MUD), and contours are drawn at intervals of 2 MUD for S_1 and S_2 and 3 MUD for S_3, starting at the first interval. Importantly, these contours should not be interpreted as confidence levels, as they identify clusters of orientations that deviate from a uniform distribution rather than confidence regions of the mean orientation.

Because the Kamb contour levels do not represent confidence intervals, we additionally quantify the angular dispersion of the inversion solutions. For each principal stress direction, we compute the angle θ_i between the axis of the i-th solution and the corresponding eigenvector of the Euclidean mean stress tensor,

$$\theta_i = \arccos\left(|\mathbf{v}_i \cdot \bar{\mathbf{e}}|\right), \tag{5}$$

where $\mathbf{v}_i$ is the unit vector of the principal stress axis and $\bar{\mathbf{e}}$ is the corresponding unit eigenvector of $\bar{\mathbf{S}}$, i.e., one of the three mean principal stress axes. The absolute value accounts for the axial (undirected) nature of principal stress orientations, for which $\mathbf{v}$ and $-\mathbf{v}$ describe the same axis. We summarize the

dispersion of the admissible solutions by the median of θ_i over all $i = 1, \ldots, N$, denoted $\tilde{\theta}$ (median angular deviation). This parameter quantifies the spread of the admissible stress tensors and is not a confidence interval on the mean stress tensor.

Additionally, we evaluate the stress ratio parameter A_ϕ (Simpson, 1997) for each admissible stress tensor. A_ϕ describes the relative magnitudes of the principal stress components and specifies the stress regime:

$$A_\phi = (n + 0.5) + (-1)^n(\phi - 0.5), \tag{6}$$

where the stress ratio ϕ is given by Eq. (1) and $n = 0$ for normal faulting ($A_\phi < 1$), $n = 1$ for strike-slip faulting ($1 < A_\phi < 2$), and $n = 2$ for reverse faulting ($A_\phi > 2$). This classification originates from the Andersonian stress states, in which one principal stress is vertical (Anderson, 1951). Since the principal axes inferred from the inversion are generally inclined, we use the terms normal, strike-slip, and reverse faulting in the generalized sense of Zoback (1992), who assigns the stress regime according to the plunges of the principal axes rather than requiring one of them to be exactly vertical. For the computation of A_ϕ, we assign n according to the most steeply plunging principal stress. The histograms presenting A_ϕ show the number of admissible stress tensors per bin as a percentage of all stress tensors in the computational grid.

4 Results

In the following sections, we describe the inversion results for test interval 1 in detail. We then present the complete stress profile derived from nine of the 11 conducted test intervals. The two remaining intervals (7 and 8), located within the MC fault zone, were excluded because the injection pressures were insufficiently high to reliably estimate fracture normal stress from reopening behavior, which is a prerequisite for the stress inversion.

4.1 Test interval 1: injection protocol and fracture kinematics

The injection protocol for test interval 1 is shown in Fig. 3a. A total of 250 L of water was injected during the test. The injection sequence began with six injection cycles at progressively increasing constant flow rates, each lasting from less than one minute to several minutes. This was followed by two step-rate tests. Between the two step-rate tests, the SIMFIP probe was unclamped and reinstalled to ensure it was properly coupled to the borehole wall, as there were concerns that it had not been adequately clamped during the initial installation. In the first step-rate test (cycle 7), the interval pressure shows a clear breakdown (pressure peak) at around 28.3 MPa (measured uphole). Based on the displacement

measurements, we interpret this breakdown as permanent shear deformation, possibly caused by fracture propagation or breaking of cohesion in the form of asperities, as also indicated by the lower pressures observed during subsequent injection steps at equal or higher flow rates.

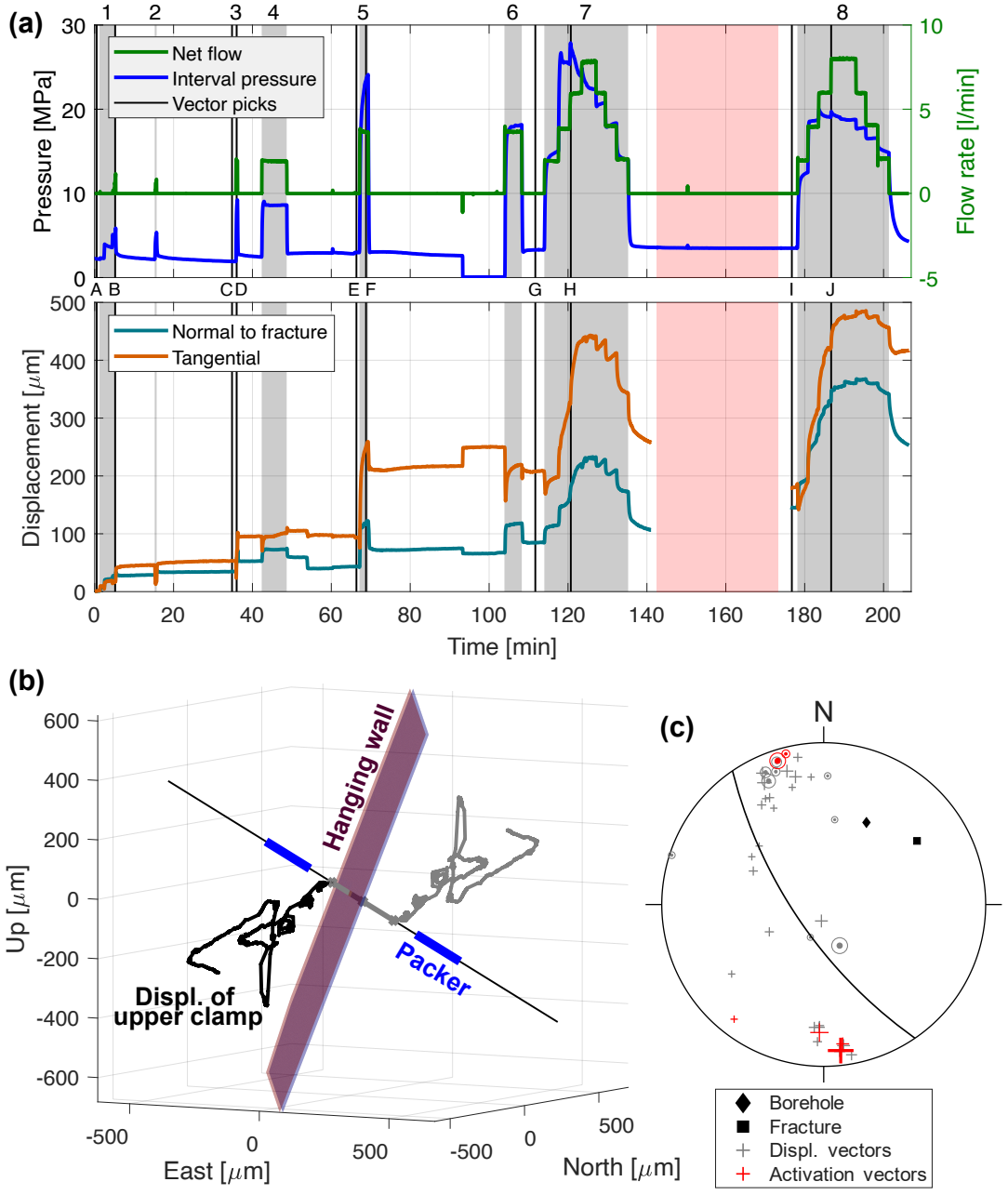


Figure 3: a) Injection protocol and measured displacement projected onto the fracture plane. Pressure and flow rate were measured uphole. Gray shading indicates the main injection cycles, numbered above the panel. The red-shaded period marks a technical interruption during which the SIMFIP had to be unclamped. Vertical lines, labeled alphabetically, correspond to incremental activation vector picks. b) 3D displacement plot showing the fracture plane, SIMFIP packers, and movement of the upper (black) and lower (gray) clamps. c) Lower-hemisphere, equal-angle stereonet of displacement vectors. All picked displacement vectors are shown in gray. Additionally, the incremental activation vectors corresponding to the picks in panel (a) are shown in red. The activation vector (thick red symbol) is calculated as the sum of these vectors. Crosses (+) denote vectors with a downward component, whereas circles with a central dot (⊙) denote vectors with an upward component.

To identify the fracture activated during fluid injection, ATV logs acquired before and after the injection were compared. The reactivated fracture was identified based on the enhanced continuity and reduced amplitude of its signature in the post-injection log as well as evidence of borehole dislocation (Bröker et al., 2026; Soom et al., 2026). The fracture has an orientation of 238°/70° (dip direction/dip). Weaker changes are also evident in the ATV travel time data, suggesting that changes in the borehole wall geometry have been caused by fracture slip. Bröker et al. (2026) used these changes in travel time to estimate permanent fracture slip and derive slip vectors.

Fig. 3b shows the relative movement of the fracture's hanging wall (upper clamp) with respect to the footwall (lower clamp). The measured displacement is decomposed into fracture normal (opening and closure) and fracture tangential (shear) components (Fig. 3a). The mechanical fracture response during fluid injection is characterized by progressive shear displacement, accompanied by fracture opening as pressure increases and subsequent closure as pressure decreases. An elastic tangential deformation component is also observed, as the tangential displacement partially recovers during shut-in as fluid pressure declines, particularly during the higher-pressure cycles 5, 7, and 8. The inferred slip is dominated by left-lateral strike-slip motion with a minor dip-slip component. The final residual displacement is uncertain because the SIMFIP probe had to be unclamped before the end of the experiment. For a more detailed discussion of the SIMFIP displacement measurements for this test, the reader is referred to Bröker et al. (2026).

The incremental displacement vectors for test 1 are shown in a stereographic projection in Fig. 3c. The majority of vectors cluster within a narrow region of the stereonet, with only a few outliers. Fig. 3a indicates the points in the injection protocol at which we interpreted non-elastic fracture activation. The corresponding incremental activation vectors are shown as red symbols in Fig. 3c. Despite the SIMFIP probe being unclamped and reinstalled between the two step-rate cycles, the incremental activation vectors exhibit a consistent orientation, characterized by a shallow plunge and an approximately N–S trend. The only exception is the vector from cycle 1, which is oriented more toward SE. This may reflect the influence of near-wellbore stress perturbations during the early stages of injection, when fluid pressures were still low. Overall, the consistent orientation of the incremental activation vectors during repeated pressurization suggests that the intermediate unclamping did not significantly affect the measurements.

The sum of the incremental activation vectors defines the activation vector, which for test 1 exhibits a dominant left-lateral strike-slip component with minor normal opening and an orientation of 174°/6° (trend/plunge; Fig. 3c). Since the estimated activation vector contains both tangential and normal displacement relative to the fracture plane, we consider only its tangential component, i.e., the projection of the vector onto the fracture plane, for the stress inversion. This choice follows from the Wallace–Bott hypothesis, according to which the slip direction corresponds to the direction of maximum resolved

shear stress on the fracture plane, while the normal displacement component associated with fracture opening does not directly constrain the stress orientation. The projected activation vector of test 1 has an orientation of 153.7°/14.5° (trend/plunge; Table 2 and Fig. 6). Throughout this study, all activation vectors are reported as the relative movement of the hanging wall with respect to the footwall.

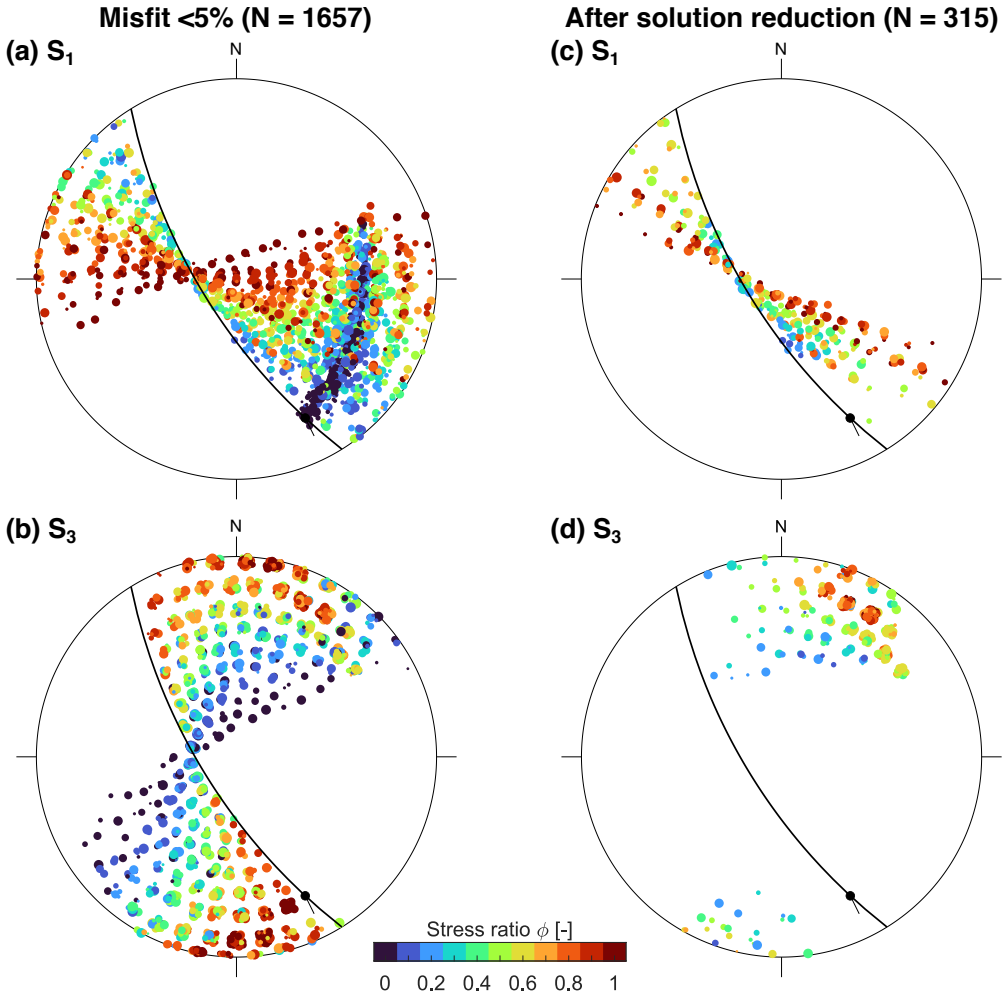


Figure 4: (a, b) Lower-hemisphere, equal-angle stereonets showing principal stress orientations (S_1, S_3) that reproduce the projected activation vector of test 1 with a misfit angle of 5° or less. Panels (c, d) show the admissible set after application of the solution-reduction procedure. A random perturbation of up to ±2° in trend and plunge was applied to all stress orientations to improve visual separation of overlapping solutions. The reactivated fracture is shown as a great circle with the projected activation vector. Stress orientations are color-coded by stress ratio ϕ, and marker size scales inversely with the misfit angle, i.e., larger symbols indicate better agreement between predicted and observed slip directions.

4.2 Test interval 1: stress inversion results

Applying SIMFIPinv to the projected activation vector of test 1 yields 1657 reduced stress tensors that explain the measured activation vector. Fig. 4a,b show the corresponding orientations of S_1 and S_3, respectively. The orientations are colored according to the stress ratio ϕ, and the marker size indicates the misfit, i.e., the angle between the predicted slip direction and the projected activation vector, with

larger symbols indicating a smaller misfit. The wide spread of solutions demonstrates that a wide range of stress orientations and stress ratios can reproduce the measured activation direction. The second solution reduction step further reduces the number of possible solutions to 315 admissible stress tensors, which are visualized in Fig. 4c,d. The spread of remaining stress tensors is substantially reduced; however, the orientations of S_1 and S_2 remain distributed along great circles (girdle pattern) on the stereonet, whereas S_3 is confined to a smaller region. This indicates that the inversion provides a stronger constraint on the orientation of S_3 than on those of S_1 and S_2, which is also consistent with a stress regime where $S_1 \approx S_2$.

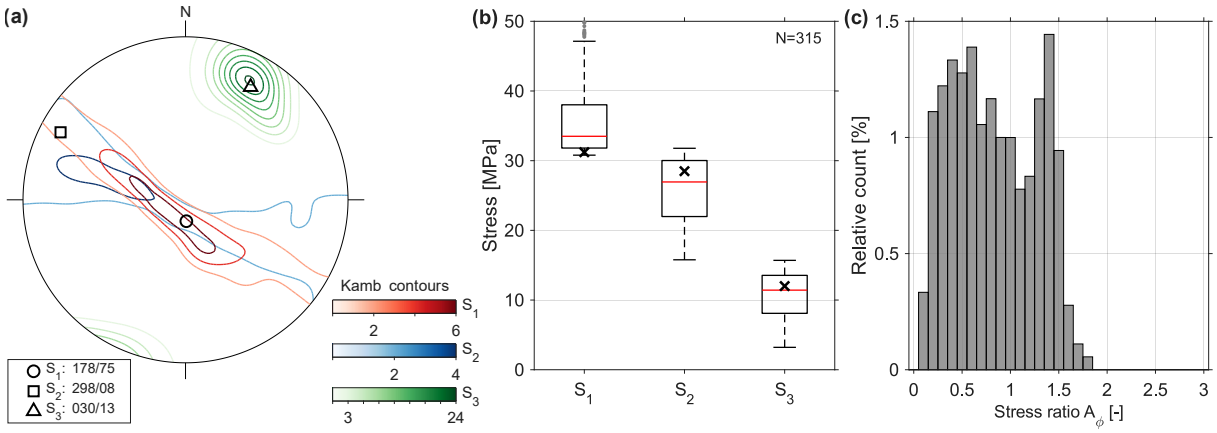


Figure 5: Summary of the stress inversion results for test interval 1. a) Lower-hemisphere equal-angle stereonet showing the orientations of the principal stress axes of the admissible stress tensors after the two solution reduction steps. Contours represent the density of principal stress orientations estimated using the modified Kamb contouring method with exponential smoothing. Higher contour levels indicate regions where stress orientations are more densely clustered. The Euclidean mean stress tensor is shown as black symbols. b) Boxplots of the corresponding principal stress magnitudes. Boxes indicate the interquartile range, the horizontal red line marks the median, whiskers extend to 1.5 times the interquartile range, and gray points denote outliers. The crosses indicate the principal stress magnitudes of the Euclidean mean stress tensor. c) Histogram of the stress ratio parameter A_ϕ for the admissible stress tensors.

Fig. 5 provides an overview of the principal stress axes of the admissible stress tensors after both solution reduction steps for test interval 1. The Euclidean mean stress tensor indicates a near-vertical S_1 orientation (178°/75°, trend/plunge), while S_2 and S_3 are oriented subhorizontally. As noted above, the orientations of S_1 and S_2 have substantially greater uncertainty than that of S_3, with both stress axes distributed along a great circle on the stereonet (girdle pattern). Consequently, both normal faulting (S_1 subvertical) and strike-slip faulting (S_2 subvertical) are possible solutions. The Euclidean mean stress tensor corresponds to a normal-faulting regime, with S_2 oriented towards WNW at 298°/8°. In contrast, the orientation of S_3 is comparatively well constrained, with the Euclidean mean indicating a NNE trend of 30°/13°. The different constraints on the principal stress axes are quantified by the angular dispersion of the admissible stress tensors. The median angular deviation $\tilde{\theta}$ of the solutions from the corresponding eigenvectors of the Euclidean mean stress tensor is 11.9° for S_3, compared with 35.8° for S_1 and 40.0° for S_2. The value for S_3 is close to the 8.3° ± 1° spacing of the S_3 directions in the search grid, indicating that its orientation approaches the best resolution achievable with the inversion grid.

Fig. 5b summarizes the distributions of principal stress magnitudes using boxplots, showing the median, interquartile range, and outliers, with the Euclidean-mean magnitudes additionally indicated. The median principal stress magnitudes are 33.5 MPa, 26.9 MPa, and 11.4 MPa for S_1, S_2, and S_3, respectively. The corresponding interquartile ranges are 6.2 MPa for S_1, 8.0 MPa for S_2, and 5.4 MPa for S_3, indicating that S_2 exhibits the largest variability in magnitude, whereas S_3 is the most constrained. The principal stress magnitudes of the Euclidean mean stress tensor are 31.2 MPa, 28.5 MPa, and 12.0 MPa for S_1, S_2, and S_3, respectively. Compared with the medians, the Euclidean mean yields a smaller S_1 and a larger S_3 magnitude, and the separation between S_1 and S_2 is reduced from 6.6 MPa to 2.7 MPa. The separation between S_2 and S_3 is comparatively large (16.5 MPa), i.e., S_2 is close in magnitude to S_1.

Fig. 5c shows the distribution of the stress ratio parameter A_ϕ, with most admissible stress tensors falling between 0.1 and 1.5. This reflects the ambiguity between normal-faulting solutions (A_ϕ = 0–1) and strike-slip solutions (A_ϕ = 1–2), reiterating that either S_1 or S_2 may correspond to the most steeply plunging principal stress. The Euclidean mean stress tensor has an A_ϕ value of 0.86.

4.3 Stress profile across all intervals

All remaining test intervals were processed using the same workflow as described above for interval 1. Intervals 7 and 8, located within the MC fault zone, were excluded because injection pressures remained below 9 MPa and were insufficiently high to estimate fracture normal stress from reopening behavior. This is consistent with the high in situ permeability of the fault zone, with mean values between 5.6×10^{-16} and 1.6×10^{-11} m^2 (Schaber et al., 2026). Six of the nine remaining tests targeted one or more pre-existing fractures. In intervals containing multiple fractures, the ATV logs did not allow unambiguous identification of the fracture reactivated during the test. Given the similar strikes and dips of the candidate fractures within each interval, the mean fracture orientation for each interval was used as the input for the inversion. Table 2 summarizes the measured activation vectors, their projections onto the fractures, the associated clamp configurations, and the inferred sense of the hanging-wall movement for the nine test intervals included in the stress profile. Fig. 6 shows these activation vectors and fractures in lower-hemisphere, equal-angle stereonets. Table 3 compiles the fracture geometry and stress magnitudes used as SIMFIPinv input parameters for the nine intervals.

Three intervals targeted intact rock sections (tests 5, 10, and 11), for which the inversion was performed using the induced hydraulic fracture. Interval 6 represents a further special case, in which an induced hydraulic fracture intersected multiple pre-existing fractures. The acoustic televiewer logs for all intervals can be found in Soom et al. (2026). In tests 5, 10, and 11 the hydraulic fractures did not form between the

Table 2: Measured and projected activation vectors, clamp configurations, and inferred movement of the hanging wall for the nine test intervals included in the stress inversion. Activation vectors are reported as the movement of the hanging wall relative to the footwall, with trend given relative to geographic North. NF = normal and RF = reverse sense of the dip-slip component, HW = hanging wall, FW = footwall

Test	Activation vector (trend/plunge) [°]	Projected activation vector (trend/plunge) [°]	Clamp location relative to fracture	Movement of hanging wall
1	174/6	154/14	Upper clamp on HW	NF
2	295/58	311/43	Upper clamp on FW	NF
3	187/-6	149/13	Upper clamp on HW	NF
4	170/24	107/64	Upper clamp on HW	NF
5	349/-20	060/-42	Both clamps on HW, fracture above	RF
6	254/38	203/50	Upper clamp on HW	NF
9	311/-3	275/22	Upper clamp on FW	NF
10	149/23	085/8	Both clamps on FW, fracture below	NF
11	353/-18	282/-48	Both clamps on FW, fracture above	RF

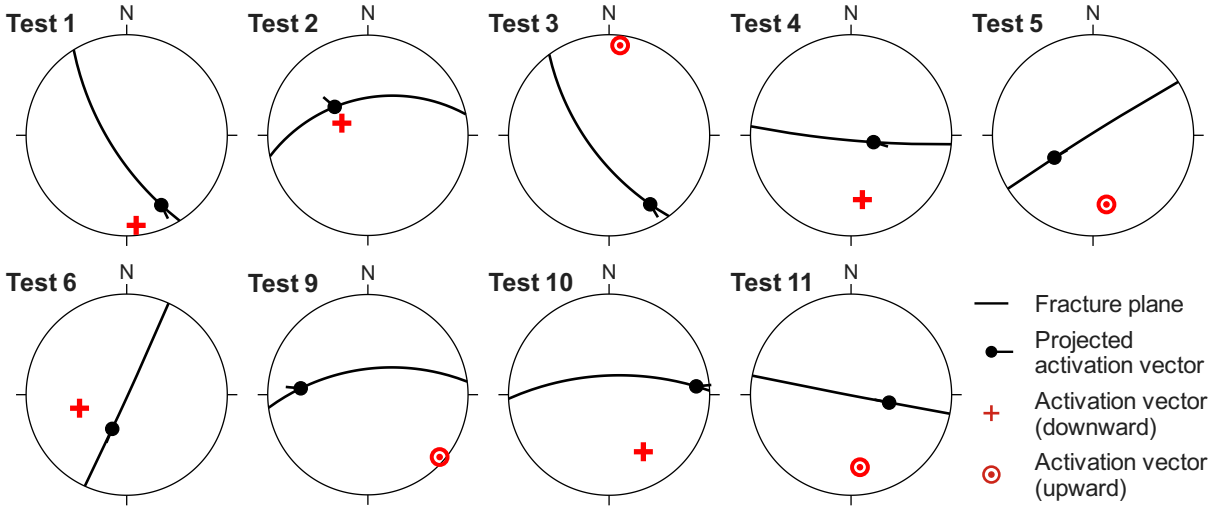


Figure 6: Overview of reactivated or created fractures and activation vectors of all test intervals in lower-hemisphere equal-angle stereonet. Crosses (+) denote vectors with a downward component, whereas circles with a central dot (⊙) denote vectors with an upward component. In addition, the activation vector is projected onto the fracture plane.

SIMFIP clamps: in tests 5 and 11 they formed behind the upper packer, whereas in test 10 the fracture was located close to the lower packer and thus outside both clamps. As a consequence, the measured displacements in these intervals do not directly describe the relative movement of the hanging wall, and the activation vectors had to be corrected before they could be used as inversion input.

Throughout this study, activation vectors are reported as the movement of the hanging wall relative to the footwall. The SIMFIP probe, however, measures the displacement of the upper clamp relative to the lower clamp. The measured vector therefore corresponds to our convention only if the upper clamp is located on the hanging wall and the lower clamp on the footwall. In the other cases, the sense of the activation vector was reversed, i.e., 180° was added to its trend and the sign of its plunge was reversed.

Table 3: Fracture orientation, projected activation vector, and estimated stress magnitudes used as SIMFIPinv input for the nine test intervals included in the stress inversion. The fracture normal stresses include the hydrostatic pressure of the fluid column, as the injection pressures were recorded uphole (Appendix C). Fracture orientations and activation vectors are given relative to geographic North.

Test	Vertical stress magnitude, S_v [MPa]	Fracture normal stress, S_n [MPa]	Fracture orientation (dip direction/dip) [°]	Projected activation vector (trend/plunge) [°]
1	30.2	15.8	238.2/69.8	154/14
2	30.2	14.8	347.9/49.4	311/43
3	30.1	13.5	233.5/66.3	149/13
4	30.0	10.5	185.1/84.2	107/64
5	29.9	16.5	327.9/87.7	060/-42
6	29.8	17.8	114.6/88.6	203/50
9	29.6	12.1	352.5/61.2	275/22
10	29.5	11.4	357.7/68.4	085/8
11	29.4	18.0	190.9/89.2	282/-48

Three clamp configurations occur in our data set (Table 2):

1. The fracture intersects the borehole between the clamps and the upper clamp is located on the hanging wall (intervals 1, 3, 4, and 6). The measured vector was used without modification.

2. The fracture intersects the borehole between the clamps and the upper clamp is located on the footwall (intervals 2 and 9). The measured vector describes the movement of the footwall relative to the hanging wall and was therefore reversed.

3. The fracture is located outside the deformation cage, so that both clamps are on the same fracture wall (intervals 5, 10, and 11). Here the two clamps sample the displacement of the same block, whose magnitude decreases with distance from the fracture plane. The differential measurement is consequently dominated by the clamp closer to the fracture: if this is the upper clamp, the measured vector points in the direction of the block movement, whereas if it is the lower clamp, it points in the opposite direction. The activation vector was reversed whenever the resulting sense corresponds to footwall rather than hanging-wall movement (interval 11). No correction was required for intervals 5 and 10.

Interval 6 requires an additional assumption. In this interval, the ATV logs show that the induced hydraulic fracture crosscuts several pre-existing fractures at a high angle without being noticeably deflected or arrested by them, suggesting that it propagated largely independently of the pre-existing fractures. The induced hydraulic fracture strikes nearly parallel to the borehole (fracture strike = 24.6°, borehole azimuth = 30.9°) and is close to vertical (dip = 88.6°), so that the borehole axis lies almost within the fracture plane and the distinction between hanging wall and footwall becomes difficult. We interpret the upper clamp to lie on the hanging wall and use the measured activation vector, because the resulting stress tensor is consistent with that of the neighboring interval 5.

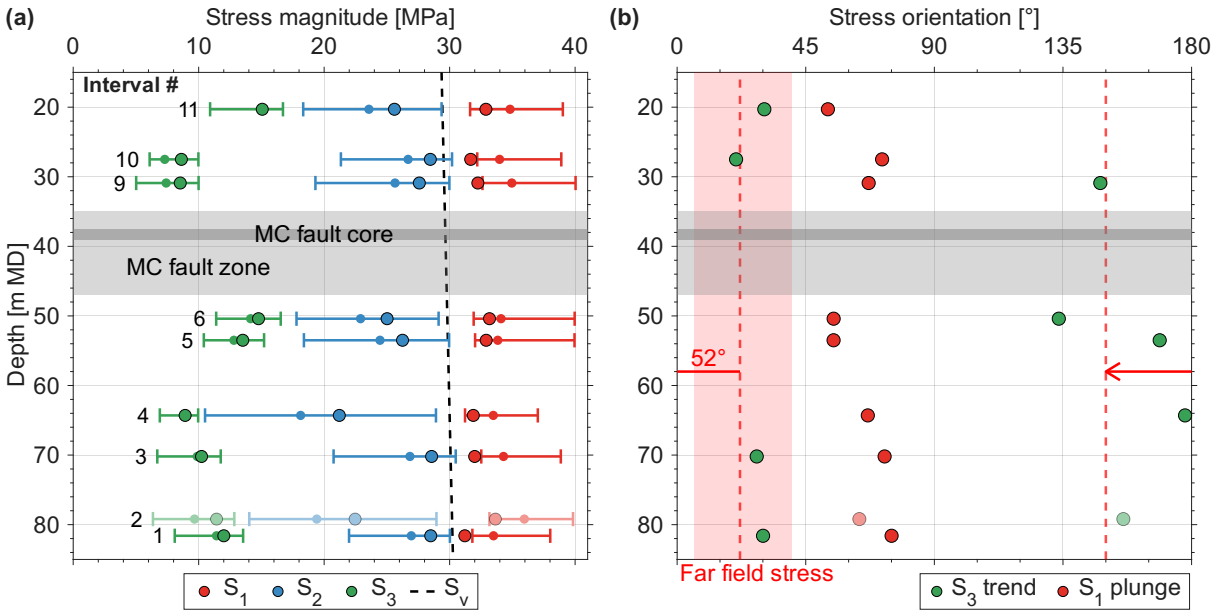


Figure 7: Results of the SIMFIP stress inversion along borehole BFE_A_05. (a) Principal stress magnitudes and estimated vertical stress S_v (dashed black line). Large symbols with black outlines denote the principal stress magnitudes of the Euclidean mean stress tensor, while small symbols and horizontal bars denote the median and the interquartile range (25th–75th percentile) of the admissible solutions, respectively. (b) Trend of S_3 and plunge of S_1 of the Euclidean mean stress tensors. S_3 trends are shown in the range 0°–180°. The red shaded area indicates the range of far-field S_{hmin} orientations (corresponding to S_3) after Bröker et al. (2024) and the red dashed line the mean S_3 orientation of N22°E. The red arrows mark the rotation of the stress around the fault zone. In both panels, the light and dark gray shading mark the MC fault zone and fault core, respectively. Results of interval 2 are shown semi-transparent, as they are considered unreliable and are not interpreted (see text).

After the two solution reduction steps, the number of admissible stress tensors ranges from 173 (interval 10) to 620 (interval 2) (Table 4). Fig. 7a shows the inversion results of the principal stress magnitudes along the borehole. Interval 2 shows an anomalous response and is not interpreted (see below). Unless stated otherwise, the ranges given in the text therefore exclude interval 2. Overall, the inferred stress magnitudes show only limited variability between the test intervals. The Euclidean-mean principal stress magnitudes range from 31.2 to 33.2 MPa for S_1, 21.2 to 28.6 MPa for S_2, and 8.5 to 15.1 MPa for S_3. The interquartile ranges of the principal stress magnitudes are comparable between intervals, spanning 5.8–8.0 MPa for S_1, 8.0–18.4 MPa for S_2, and 3.1–5.8 MPa for S_3. As mentioned previously for interval 1, S_2 is the least constrained and S_3 the best constrained magnitude in every interval. In all intervals the vertical stress falls between the mean S_1 and S_2 magnitudes, i.e., the vertical direction is not a principal direction of the Euclidean mean tensor, and S_1 exceeds S_v by 1.0–3.5 MPa because it plunges 53°–75° rather than vertically (Fig. 7b, Fig. 8a). The stress ratio A_ϕ of the Euclidean mean stress tensors varies between 0.54 and 0.86 (Fig. 8b). These mean tensors therefore indicate a normal faulting regime for all test intervals. The admissible sets, however, also include a considerable number of tensors corresponding to a strike-slip regime, as visible in the A_ϕ distributions in Fig. 8b, which reflects the weak constraint on the orientations of S_1 and S_2. In intervals 5, 6, and 11, the S_1

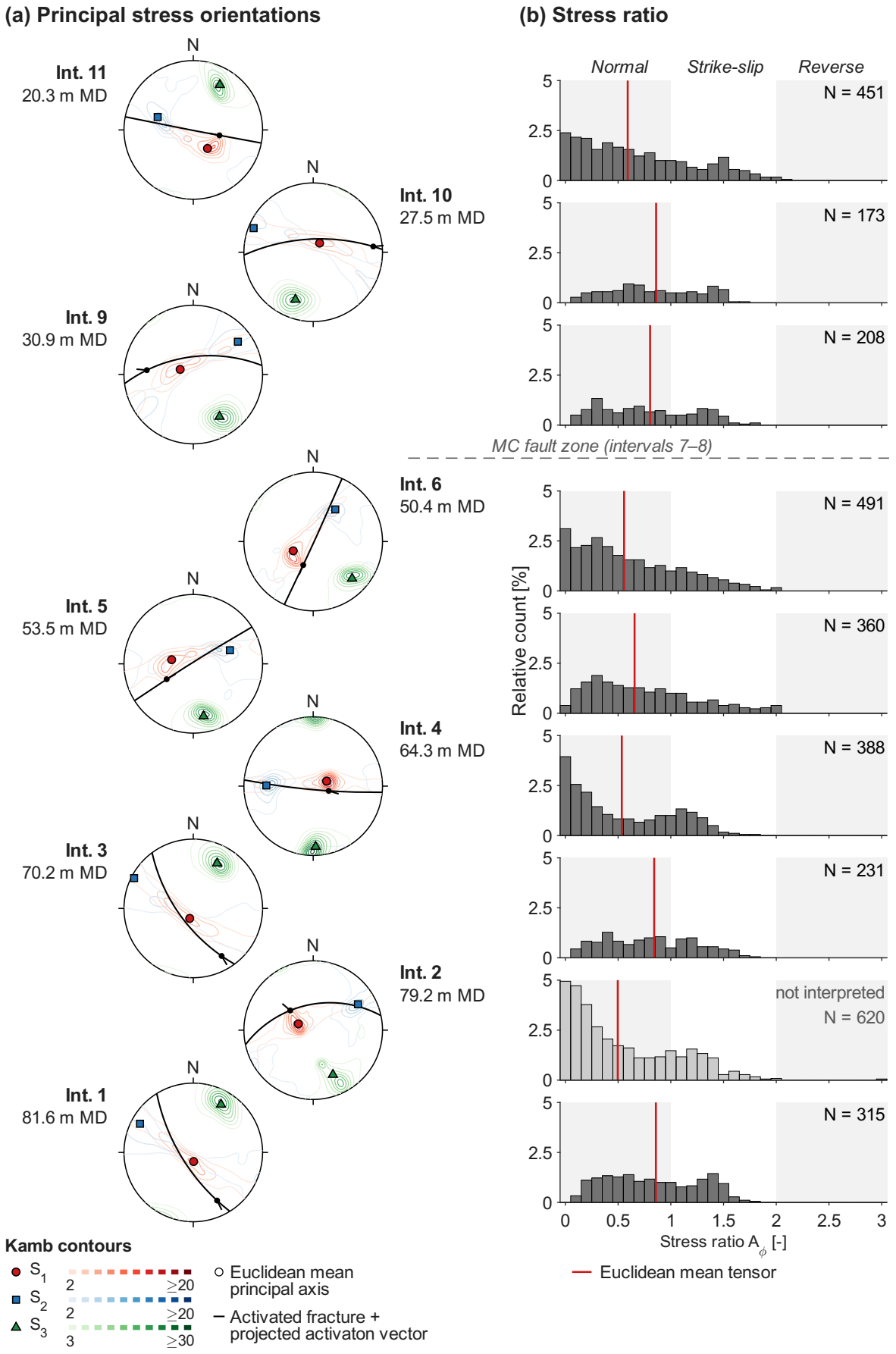


Figure 8: Results of the SIMFIP stress inversion along borehole BFE_A_05. (a) Lower-hemisphere equal-angle projections of the principal stress orientations as in Fig. 5a, with contour levels identical for all intervals. The fracture plane (great circle) and the activation vector projected onto it are shown. (b) Distribution of the stress ratio A_ϕ as in Fig. 5c. The red line marks A_ϕ of the Euclidean mean stress tensor.

plunge of 53°–55° of the mean tensor lies close to the threshold of 52° below which the stress state is classified as transtensional (Zoback, 1992). This proximity to transtension reflects the inclination of the principal axes rather than the stress magnitudes, since these intervals do not show elevated A_ϕ values.

Interval 2 shows an anomalous response and is excluded from the interpretation of stress orientations. Its Euclidean-mean S_3 trend deviates by 52°–54° from those of the immediately adjacent intervals 1 and 3, which themselves agree to within about 2°. It is also the interval for which the solution reduction retains the largest number of stress tensors (620). In this interval, we targeted a large open fracture visible in the ATV log prior to the test. The SIMFIP clamps were positioned above and below this structure, but during pressurization we measured fracture closure, i.e., a decreasing distance between the clamps. We cannot explain this observation with certainty and hypothesize that the targeted structure either changes its orientation away from the borehole wall or is hydraulically connected to one or more fractures of different orientation.

Because the stress inversion constrains S_3 considerably better than S_1 and S_2, we base the description of the stress orientations along the borehole on the S_3 axis of the Euclidean mean stress tensors. In all intervals S_3 is subhorizontal, with plunges between 8° and 19° (excluding interval 2; Table 4, Fig. 7b), so that the variation along the borehole is essentially a rotation about the vertical axis that can be described by the S_3 trend alone for simplification. Relative to the far-field S_3 azimuth of N22°E (red dashed line in Fig. 7b), implied by the S_{Hmax} orientation (with S_{Hmax} corresponding to S_2) estimated from mini-frac tests in the nearby Bedretto geothermal testbed (Bröker et al., 2024), the deep intervals 1 (81.6 m MD) and 3 (70.2 m MD) fall within the range of observed far-field S_3 orientations. Towards the MC fault zone, S_3 rotates counterclockwise and its deviation from the far-field azimuth increases progressively, reaching 24° in interval 4 (64.3 m MD), 33° in interval 5 (53.5 m MD), and 68° in interval 6 (50.4 m MD), the interval closest below the fault zone. Interval 9 (30.9 m MD), the closest interval above the fault zone, deviates by 54°, whereas intervals 10 (27.5 m MD) and 11 (20.3 m MD) are again aligned with the far-field direction. With median angular deviations $\tilde{\theta}$ of all admissible S_3 solutions between 8.4° and 15.3° within each interval (Table 4), the rotations of up to 68° observed towards the MC fault zone clearly exceed the dispersion of the admissible solutions and therefore cannot be explained by the uncertainty of the inversion alone. The stress orientations along the profile therefore indicate an average counterclockwise rotation of S_3 by about 52° (mean of intervals 5, 6, and 9) associated with the intersected fault zone. This rotation is asymmetric: below the fault zone the S_3 trend returns gradually towards the far-field orientation over several meters, whereas above the fault zone it recovers much more rapidly within only a few meters.

Table 4: Stress inversion results for the nine test intervals along borehole BFE_A_05. N is the number of admissible stress tensors after the two solution reduction steps. Principal stress magnitudes and orientations refer to the Euclidean mean stress tensor of the admissible solutions. Values in parentheses give the 25th and 75th percentiles (P_{25}–P_{75}) of the magnitude distribution of the admissible solutions, computed for each principal stress independently. Orientations are reported as trend/plunge relative to geographic North and $\tilde{\theta}$ is the median angular deviation of the individual solutions from the corresponding mean principal axis (Eq. (5)). A_ϕ is the stress ratio parameter of the Euclidean mean stress tensor (Eq. (6)). The mean row gives the arithmetic mean over all intervals except interval 2 (marked with a *). MD = measured depth of the interval center.

			S_1			S_2			S_3			
Test	MD [m]	N [–]	Magn. (P_{25}–P_{75}) [MPa]	Orient. [°]	$\tilde{\theta}$ [°]	Magn. (P_{25}–P_{75}) [MPa]	Orient. [°]	$\tilde{\theta}$ [°]	Magn. (P_{25}–P_{75}) [MPa]	Orient. [°]	$\tilde{\theta}$ [°]	A_ϕ [–]
1	81.6	315	31.2 (31.8–38.0)	178/75	35.8	28.5 (22.0–30.0)	298/8	40.0	12.0 (8.1–13.5)	030/13	11.9	0.86
2*	79.2	620	33.6 (33.2–39.8)	293/64	19.5	22.5 (14.0–29.0)	060/17	37.0	11.4 (6.4–12.8)	156/20	19.3	0.50
3	70.2	231	32.0 (32.5–38.9)	200/73	35.3	28.6 (20.8–30.5)	297/2	40.3	10.2 (6.7–11.8)	028/17	8.6	0.84
4	64.3	388	31.9 (31.2–37.0)	070/67	17.0	21.2 (10.5–28.9)	271/22	34.9	8.9 (6.9–10.0)	178/8	10.1	0.54
5	53.5	360	32.9 (32.0–40.0)	281/55	25.2	26.2 (18.4–30.0)	070/31	36.2	13.5 (10.4–15.2)	169/15	11.5	0.66
6	50.4	491	33.2 (31.9–40.0)	245/55	21.7	25.0 (17.8–29.1)	034/31	38.9	14.8 (11.4–16.5)	134/14	15.3	0.56
9	30.9	208	32.2 (32.6–40.0)	291/67	29.3	27.6 (19.3–30.0)	054/13	34.8	8.5 (5.0–10.0)	148/19	8.4	0.80
10	27.5	173	31.7 (32.2–38.9)	035/72	34.0	28.5 (21.3–30.2)	292/4	38.5	8.6 (6.1–10.0)	201/18	12.3	0.86
11	20.3	451	32.9 (31.6–39.0)	143/53	23.9	25.6 (18.3–29.4)	290/33	36.8	15.1 (10.9–16.7)	031/16	14.0	0.59
Mean	–	327	32.3 (32.0–39.0)	–	27.8	26.4 (18.5–29.8)	–	37.5	11.5 (8.2–13.0)	–	11.5	0.71

5 Discussion

5.1 Uncertainty of the inverted stress tensors and choice of a representative stress state

For each test interval, we take the Euclidean mean of all admissible stress tensors as the representative stress state and describe the spread of the admissible solutions by their magnitude distributions and median angular deviations ($\tilde{\theta}$). The orientation scatter of the admissible stress tensors is closely linked to the stress anisotropy. When S_1 and S_2 are similar in magnitude, the stress state lies close to the transition between normal and strike-slip faulting ($A_\phi = 1$). In this case, rotating S_1 and S_2 within their common plane (girdle pattern) hardly changes the shear stress resolved on the fracture, and thus the predicted slip direction. The inversion therefore constrains the orientations of S_1 and S_2 less well, whereas the orientation of S_3, normal to the plane containing the two other principal stresses, remains well resolved. With A_ϕ between 0.54 and 0.86, S_2 is closer in magnitude to S_1 than to S_3 in all intervals. Consistently, the median angular deviation $\tilde{\theta}$ of S_1 decreases with increasing S_1–S_2 separation of the Euclidean mean tensor, from about 35° for separations of about 3 MPa (intervals 1, 3, and 10) to 22°–25° for separations of 7–8 MPa (intervals 5, 6, and 11) and 17° for a separation of about 11 MPa (interval 4). In other words, the inversion constrains the greatest principal stress orientation better when its difference from the intermediate principal stress is larger. In contrast, the orientation of S_2 remains weakly constrained across all intervals ($\tilde{\theta}$ =35°–40°). The activation mechanism, i.e., the ratio of opening to shear displacement, does not directly affect the dispersion of any of the principal stress axes, since only the projection of the activation vector onto the fracture plane enters the inversion.

A further consideration concerns the discrepancy in stress magnitude between the Euclidean mean stress tensor and the median stress magnitudes. In all intervals, the median magnitudes, which are obtained for each principal stress independently of its orientation, yield a larger S_1, a smaller S_2, and, with the exception of interval 11, a smaller S_3 than the Euclidean mean. This agrees with the analysis of Gao and Harrison (2018, 2019), who showed that processing principal stress magnitudes and orientations separately tends to produce more extreme principal stresses than the Euclidean mean, because it ignores the connection between magnitude and orientation. We therefore use the Euclidean mean as the representative stress state, as it is unique, yields orthogonal principal axes, and preserves the tensorial nature of stress. We acknowledge that the spread in both stress orientations and stress magnitudes that can explain the measured activation vectors within the chosen misfit of 5° is considerable. In addition, the other inputs (vertical stress, fracture normal stress, and fracture orientation) are themselves uncertain, and these uncertainties were not incorporated into the inversion. Incorporating them, for example by sampling S_v and S_n within their uncertainty ranges, would provide a more complete uncertainty estimate

and will be addressed in future work.

5.2 Comparison to previous stress measurements at the BedrettoLab

Overall, the stress magnitudes inferred from SIMFIPinv are comparable between the test intervals and of the same order as previous stress measurements at the BedrettoLab. The stress magnitudes determined in this study can be compared with the mini-frac results of Bröker and Ma (2022) and Bröker et al. (2024), determined in the up to 40 m long stress measurement boreholes in and around the geothermal testbed, of which the closest is approximately 100 m from borehole BFE_A_05. The vertical stress at our test intervals, obtained by integrating the overburden (Appendix B), is 29.4–30.2 MPa and thus higher than the range of 24.1–28.6 MPa reported for the geothermal testbed (Bröker et al., 2024), reflecting the larger overburden at the Earthquake Physics testbed. Our inverted greatest principal stress S_1 (Euclidean mean: 31.2–33.2 MPa) exceeds both the local S_v and all principal stresses reported by Bröker and Ma (2022). A direct comparison is, however, limited, since Bröker and Ma (2022) assume the vertical direction to be a principal stress direction. In our inversion results, S_1 plunges 53°–75°, while S_2 and S_3 plunge 2°–33° and 8°–19°, respectively. Hence, S_2 and S_3 are not strictly equivalent to the horizontal stresses S_{Hmax} and S_{hmin} in our results. We therefore additionally computed S_{Hmax} and S_{hmin} from the Euclidean mean stress tensors following Lund and Townend (2007), whose method determines the azimuth of S_{Hmax} for stress tensors with arbitrarily oriented principal axes. This yields S_{Hmax} magnitudes of 22.7–28.6 MPa oriented between N48°E and N125°E, and S_{hmin} magnitudes of 9.3–16.2 MPa. Our S_{Hmax} magnitudes are consistent with the mini-frac estimate of 25.4 ± 2.3 MPa (Bröker and Ma, 2022). This suggests similar maximum horizontal stresses at both locations, possibly reflecting a common far-field loading. In contrast, S_{hmin} is lower than the mini-frac estimate of 14.6 ± 1.4 MPa in several intervals. Since S_{hmin} cannot be lower than S_3, this implies an even lower S_3 in these intervals and suggests a locally reduced S_3 at the Earthquake Physics testbed. S_{Hmax} remains below the vertical stress in all intervals, consistent with the normal-faulting regime indicated by the stress ratio parameter A_ϕ of the Euclidean mean stress tensors (0.54–0.86; Table 4). This regime is supported by the plunge criteria of Zoback (1992), according to which all intervals correspond to normal faulting (S_1 plunge $\geq 52°$, S_3 plunge $\leq 35°$), although intervals 5, 6, and 11 lie close to the transition to transtension. Our A_ϕ values are, however, lower than the value of 0.9 derived from the mini-frac tests in the geothermal testbed (Bröker and Ma, 2022).

Preliminary results from a mini-frac campaign in several boreholes of the Earthquake Physics testbed indicate significant spatial variations in the S_3 magnitude, ranging from 10.8 to 23.7 MPa (Kövér et al., 2026). Mini-frac intervals located farther from the MC fault, at distances of 12–38 m, generally yield higher S_3 magnitudes than those inferred in this study. In contrast, low S_3 magnitudes comparable to ours were obtained for mini-frac intervals in the vicinity of the fault, within approximately 6 m on the

northern side of the fault and 18 m on the southern side, all of which are located around a patch of the fault on the opposite side of the Bedretto Tunnel with respect to BFE_A_05. This suggests that a reduced S_3 magnitude is a general feature of the stress field around the MC fault. Full stress tensors were estimated for 32 mini-frac intervals using an inversion technique applicable to hydraulic fracturing tests in inclined boreholes (Kövér et al., 2026). Similar to our results for the intervals farther from the fault zone, most of these tensors have an S_3 orientation close to the far-field trend of N22°E and correspond to a normal-faulting regime, although a strike-slip regime is consistently obtained in some regions. A high-resolution stress profile along a borehole oriented sub-perpendicular to the MC fault reveals rotations of the S_3 axis resembling those observed in BFE_A_05. The inverted mini-frac intervals also include the hydraulic fractures of SIMFIP intervals 5, 6, and 10, for which the two inversion methods agree reasonably well; a detailed comparison is given in Kövér et al. (2026).

Although located about 300 m from BFE_A_05, the borehole array analyzed by Wang et al. (2026) in the geothermal testbed provides an independent estimate of local stress heterogeneity in the Rotondo granite, derived from the inversion of borehole ellipticity from eight boreholes of 190–400 m length. Their S_{Hmax} azimuths, which mostly range from N60°E to N130°E, are comparable to the N48°E–N125°E obtained in this study. Both data sets indicate a normal-faulting regime with A_ϕ values of 0.54–0.86 from the SIMFIP stress inversion and an average of about 0.6 from ellipticity (Wang et al., 2026), both below the value of 0.9 derived from mini-frac tests in the geothermal testbed (Bröker and Ma, 2022). Most notably, both methods yield principal stress tensors that are markedly oblique at the local scale, with S_1 deviating by 15°–37° from the vertical in our results and by 0°–54° (mean 24°) in those of Wang et al. (2026). These inclinations exceed those inferred from hydraulic fracture traces of mini-frac tests (0°–10°) (Bröker et al., 2024) and from breakouts at the margins of a major fault zone in the same borehole array (12°–18°) (Zhang et al., 2023). Part of this obliquity may be of topographic origin, since regional modeling predicts non-vertical principal stresses down to about 1.5 km below surface in the Bedretto area (Hamdi et al., 2025). However, a topographic effect would vary smoothly over the scale of the Earthquake Physics testbed and cannot explain the variability of the S_1 plunge between neighboring intervals.

5.3 Stress rotation and magnitude variations across a fault zone

We observed a counterclockwise rotation of S_3 by 52° on average adjacent to the MC fault zone relative to the far-field stress state around the BedrettoLab (Bröker et al., 2024). This rotation is asymmetric: below the fault zone, S_3 remains rotated by 24° about 17 m from its lower end (interval 4) and returns to the far-field orientation only about 23 m from it (interval 3), whereas above the fault zone the rotation recovers between 4.1 m (interval 9) and 7.5 m (interval 10). Because of the discrete spacing of the test intervals, these distances only bracket the extent of the perturbation and cannot resolve its exact dimensions. In

terms of magnitude the situation is less clear, but our results suggest a lower differential stress directly below the fault zone and a higher one directly above it. Below the fault zone, $S_1 - S_3$ increases from 18.4 MPa in interval 6 to 23.0 MPa in interval 4, whereas above it, intervals 9 and 10 (23.1–23.7 MPa) exceed interval 11 (17.8 MPa). Since S_1 remains nearly constant along the profile, this variation results mainly from S_3. Similarly, A_ϕ is reduced in intervals 4–6 (0.54–0.66) but not in intervals 9 and 10 (0.80–0.86). Some variability in stress ratio between intervals nevertheless exists irrespective of their distance to the fault zone, as shown by the low A_ϕ of 0.59 in interval 11, the interval farthest above it. Moreover, the differences in differential stresses are smaller than the interquartile ranges of the admissible solutions, so we regard them as a tendency consistent with the asymmetric rotation.

The observed asymmetry is consistent with the internal architecture of the fault zone in BFE_A_05, where the fault core lies in its upper part and is bounded by about 2.5 m of fractured rock above, measured along the borehole trajectory, and 8 m below (Schaber et al., 2026). A wider zone of compliant and fractured rock on one side of the fault core may extend the stress perturbation further into the adjacent host rock. Rotations of S_3 resembling those in BFE_A_05 were also inferred from mini-frac tests along a borehole oriented sub-perpendicular to the MC fault (Kövér et al., 2026), indicating that the stress perturbation is not restricted to the vicinity of BFE_A_05.

Such local stress perturbations around faults and fractures are not unusual. Borehole observations have documented rotations of principal stresses or breakout orientations over distances of decimeters to a few meters adjacent to individual fractures and faults (Barton and Zoback, 1994; Lin et al., 2010; Sahara et al., 2014; Zhang et al., 2023), and over distances of several to tens of meters across fault and shear zones (Shamir and Zoback, 1992; Valley and Evans, 2010; Krietsch et al., 2019; Talukdar et al., 2022; Zhang et al., 2023), often accompanied by local variations of the stress magnitudes (Chang and Jo, 2015; Krietsch et al., 2019; Talukdar et al., 2022). The extent of the perturbation of about 4–23 m observed in BFE_A_05 therefore lies within the range reported for fault-zone-related stress perturbations.

Stress variations in and around fault zones, expressed as rotations of the principal stresses and changes in their magnitudes, have also been simulated in numerical studies at different scales (e.g., Reiter, 2021; Ziegler et al., 2024). These studies point to two main mechanisms for such stress perturbations: slip on faults and fractures (Barton and Zoback, 1994; Zhang and Ma, 2021) and a reduction of the elastic moduli within the damage zone (Faulkner et al., 2006; Healy, 2008; Ziegler et al., 2024). Both mechanisms are coupled, since the fracture density increasing towards the fault core facilitates slip and at the same time reduces the elastic moduli of the rock mass (Zhang and Ma, 2021). Zhang and Ma (2021) showed that in 2D multilayer models, in which the density of randomly oriented frictional fractures increases towards the fault core, slip on these fractures progressively reorients the greatest principal stress towards a limiting angle of 45° with the fault plane, while the differential stress decreases. At the same time,

the accumulated damage decreases the effective Young's modulus and increases the Poisson's ratio of the rock mass, resulting in a compliant damage zone embedded in stiffer host rock, which by itself can also rotate the stresses (Faulkner et al., 2006; Healy, 2008; Ziegler et al., 2024). At the scale of a fault zone, both mechanisms therefore predict stress rotations that are largely confined to the fault zone (e.g., Ziegler et al., 2024) and the host rock immediately adjacent to it (e.g., Barton and Zoback, 1994).

These studies indicate that stress variability in crystalline rocks is principally controlled by three factors: (1) slip on structures, (2) stiffness variations within the damage zone and core of fault zones, and (3) interaction between structures. The interplay of these factors can produce complex patterns of stress variability, which we conceptualize in Fig. 9. Slip is the driver of the perturbation in all cases, whereas structural maturity (letters A to C) and structural interaction (numbers 1 to 3) modulate its pattern. A single shear fracture (A1 in Fig. 9) induces a relatively simple and well-established stress perturbation pattern, with compressive and extensile lobes near the fracture tips and a stress relaxation zone along the fracture walls associated with partial or complete shear stress drop. Near the fracture center, the perturbation is symmetric about the fracture plane, whereas near the tips it becomes antisymmetric, with contrasting perturbations on either side of the fracture. In particular, stress orientations near the fracture tips can vary strongly across the structure, as illustrated by the maximum principal stress trajectories in Fig. 9 A1. The extent of the perturbation is proportional to fracture size (Pollard and Segall, 1987; King et al., 1994).

With increasing structural maturity, a damage zone (B in Fig. 9) and a fault core (C in Fig. 9; see also Caine et al., 1996) develop, forming zones of reduced stiffness. These compliant zones are an additional source of stress variability, typically expressed as stress relaxation and reduced differential stress. Interaction between structures occurs either along discontinuous structures composed of distinct slip patches and relay zones (2 in Fig. 9; see also Kim et al., 2004; Choi et al., 2016) or within fracture and fault networks (3 in Fig. 9; see also Peacock et al., 2017). The former leads to stress variability along the structure, with relaxed patches separated by compressive or extensile relay zones. The latter leads to complex interactions, which can produce scale-invariant stress variability characterized by power-law spectra (Day-Lewis et al., 2010; Valley and Evans, 2010).

Within the MC fault zone, the higher fracture density reduces the compressional and shear wave velocities relative to the host rock (Schaber et al., 2026), indicating a somewhat more compliant zone. However, large stiffness contrasts, such as those required for substantial rotations in the models of Ziegler et al. (2024), are not expected, since the seismic velocity reduction measured with borehole logs is moderate (Schaber et al., 2026) and the fault zone is immature and has a weakly developed damage zone (Achtziger-Zupančič et al., 2024; Schaber et al., 2026). The stress perturbation extends about 23 m below and less than 7.5 m above the fault zone. Based on the scaling between slip-patch size and the extent of

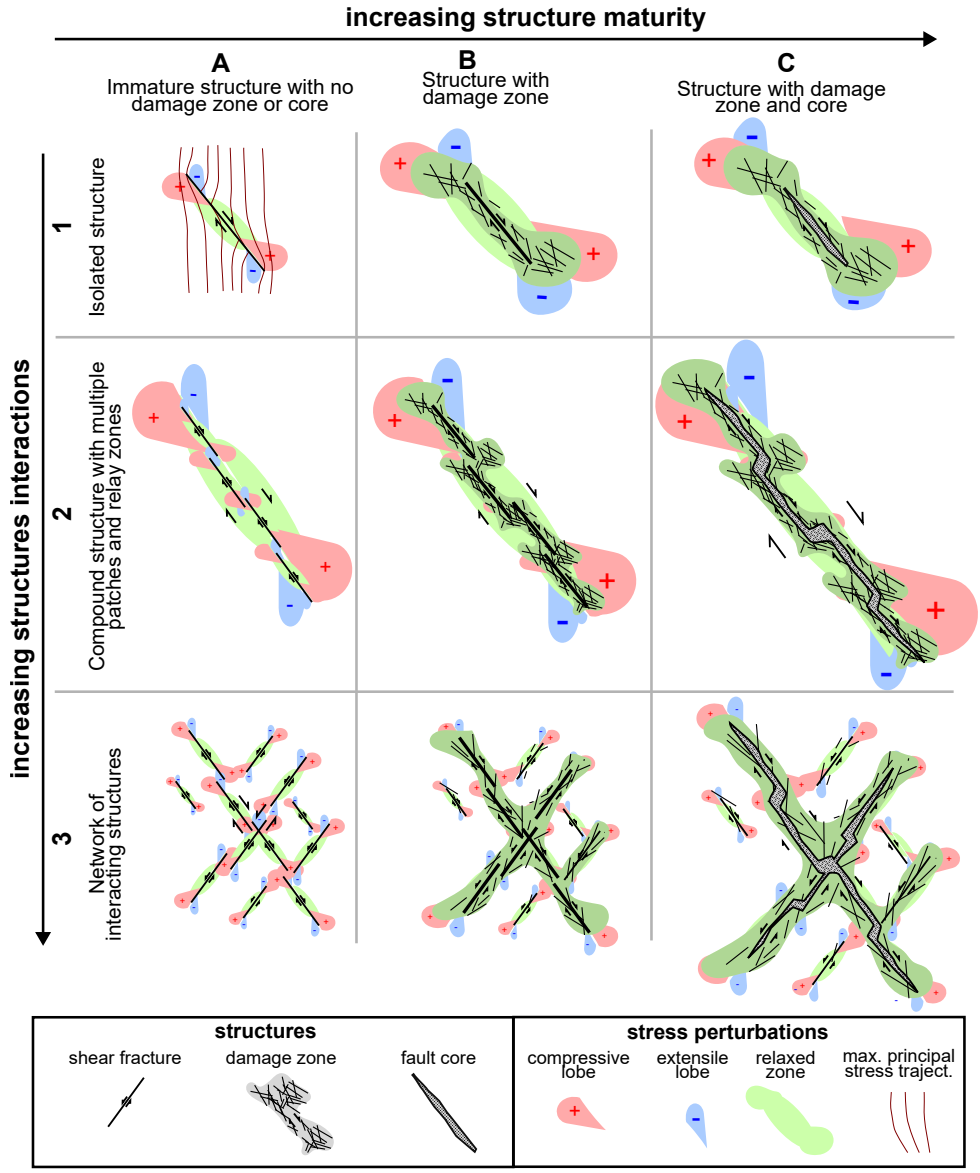


Figure 9: Conceptual representation of the factors controlling stress perturbations around structures. Columns (A–C) represent increasing structural maturity: A, structure without damage zone; B, structure with damage zone; C, structure with damage zone and core. Rows (1–3) represent increasing structural interaction: 1, single structure; 2, segmented structure with slip patches and relay zones; 3, network of structures. Stress perturbations are controlled by the combination of slip on structures, stiffness variations due to the damage zone and core, and interaction between structures.

the associated stress perturbation (Pollard and Segall, 1987; King et al., 1994), a slip patch of a diameter of about 50 m would be sufficient to explain the observed perturbation. This is considerably smaller than the MC fault zone, which extends over more than 100 m (Achtziger-Zupančič et al., 2024). Together, these observations suggest that the MC fault zone is an immature compound fault system composed of multiple slip patches connected by relay zones with a partially developed damage zone, corresponding to type A2 or B2 in Fig. 9.

As already mentioned, the behavior around the fault zone is asymmetric: below the fault zone, the predicted reduction of the differential stress is also reflected in the lower differential stress and A_ϕ of the intervals closest to the fault zone. Above the fault zone, however, neither is reduced. This asymmetry may reflect the position of the borehole relative to the slip patch: if the borehole intersects the patch away from its center, the stress perturbation sampled along the borehole is inherently asymmetric. The asymmetry is also consistent with the structure of the damage zone, in which fracture intensity decreases abruptly above the fault core but gradually over several meters below it (Schaber et al., 2026). The more extensively fractured, and therefore more compliant, rock below the fault core would be expected to accommodate a larger share of the deformation.

In the BedrettoLab, local stress perturbations consistent with this conceptual view of stress perturbation have also been observed in the geothermal testbed. First, mini-frac tests revealed a counterclockwise rotation of S_{Hmax} by up to 37° within the enlarged testbed niche compared with boreholes along the main tunnel. This rotation, together with an increased inclination of S_1, was hypothesized to result from the larger excavation of the laboratory niche and from natural fractures favorably oriented for slip (Bröker et al., 2024). Second, breakouts were observed along parts of the long boreholes in the geothermal testbed, predominantly where the boreholes cross a major fault zone (Zhang et al., 2023). Within this fault zone, the breakout azimuths rotate by up to about 35° from its margin to its center and back, over a length of about 60 m along the borehole trajectories, corresponding to the thickness of the fault zone. Forward modeling suggests that this rotation results from a decrease of the stress ratio from its far-field value of 0.9 towards the fault zone center, caused by slip on the fractures therein, combined with a clockwise rotation of S_{Hmax} by about 30° (Zhang et al., 2023). The magnitude of this fault-zone-scale rotation is comparable to that observed adjacent to the MC fault zone, but its sense is opposite, since S_3, and thus S_{Hmax}, rotates counterclockwise in BFE_A_05. The decrease of the stress ratio towards the fault zone in the geothermal testbed agrees with the lower A_ϕ of the intervals below the MC fault zone, but not with those above it. Besides the fault-zone-scale rotation, breakouts also vary at scales of several meters down to a few centimeters, and rotate towards the dip direction of the fractures they approach, which was attributed to the stress drop associated with slip on these fractures (Zhang et al., 2023). This probably reflects a combination of mechanical weakening of the rock next to the fractures (Sahara et al., 2014) and a real rotation of the stress field resulting from the stress drop linked to fracture slip (Zhang

and Ma, 2021; Zhang et al., 2023). Sub-meter rotations around individual fractures were likewise observed in the cross-sectional ellipticity of the same boreholes (Wang et al., 2026), which is insensitive to rock strength and therefore points to an actual perturbation of the stress field. However, no systematic larger-scale rotations related to the fault zones were resolved from the ellipticity inversion, possibly because a constant stress state was assumed within the chosen 25 m inversion intervals (Wang et al., 2026). These observations of stress perturbation in the geothermal testbed suggest that the situation involves interaction of multiple structures, corresponding to category A3 or B3 in Fig. 9.

5.4 Inversion of slip on hydraulic fractures

In four test intervals (5, 6, 10, and 11), hydraulic fractures were initiated and used as input for the stress inversion. In theory, these fractures should propagate perpendicular to the least principal stress (S_3), such that they are pure tensile (mode I) fractures without shear displacement. However, the SIMFIP measurements reveal a significant shear component on all four fractures. For the hydraulic fracture in interval 11, Bröker et al. (2026) independently identified a permanent shear displacement of about 0.4 mm on post-test ATV travel-time images, with a slip direction deviating by only 13° from the projected SIMFIP activation vector. Similarly, other in situ studies have shown that hydraulic fractures can propagate as mixed-mode ruptures and initiate along planes of weakness (Guglielmi et al., 2021a), while laboratory hydraulic fracturing experiments on granite have revealed varying degrees of shear failure at the microstructural scale (Li and Einstein, 2019). Bröker et al. (2026) proposed that shear displacement along hydraulic fractures could result from the coupled effects of fracture propagation and stress redistribution surrounding the inclined borehole.

In general, hydraulic fractures are not ideal to invert for the local stress tensor. Assuming they form perpendicular to the local S_3 orientation, they are unfavorably oriented for shear failure. In this configuration, the direction of the resolved shear stress on the fracture plane becomes highly sensitive to small changes in principal stress orientations or magnitudes, as well as to local perturbations caused by the borehole, nearby fractures, and lithological heterogeneity. In their sensitivity analysis, Bröker et al. (2026) show that varying the S_{Hmax} azimuth by ±45° changed the predicted Wallace–Bott slip direction by 178° on the hydraulic fracture of interval 11 and by 163° on the near-vertical pre-existing fracture of interval 4, compared with about 100° on the more favorably oriented fractures of intervals 1 and 3. Compared with the intervals targeting pre-existing fractures, the hydraulic fracture intervals show a generally larger dispersion of the admissible S_3 orientations, with $\tilde{\theta}$ of 11.5°–15.3° versus 8.4°–11.9°. Moreover, three of the four hydraulic fracture intervals (5, 6, and 11) show the most strongly inclined principal axes, with S_1 plunging close to the threshold between normal faulting and transtension (Zoback, 1992), which may partly reflect the weaker constraint provided by these fractures. Despite these

limitations, the inversion results of the hydraulic fracture intervals are broadly consistent with those of the neighboring intervals that target pre-existing fractures, and the rotation of S_3 close to the MC fault zone is also resolved by interval 9, in which pre-existing fractures were reactivated. Moreover, the results for intervals 5, 6, and 10 agree reasonably well with an independent inversion of these hydraulic fractures based on a novel mini-frac analysis by Kövér et al. (2026). Nevertheless, given the unfavorable orientation of hydraulic fractures for shear and the larger dispersion of the corresponding solutions, we consider the results from reactivated pre-existing fractures to be more robust.

6 Conclusions

Stress measurements in boreholes rarely resolve the complete stress tensor and often rely on simplifying assumptions, e.g., that one principal stress is parallel to the borehole axis. In this study, we extended the SIMFIP stress inversion method to estimate the complete three-dimensional stress tensor from fracture displacements measured with the SIMFIP probe during step-rate injection tests. The inversion is based on the Wallace–Bott hypothesis and requires as input the activation vector, the orientation of the activated fracture, the fracture normal stress, and the vertical stress. We conducted 11 injection tests along a 61 m long section of borehole BFE_A_05 at the BedrettoLab. Nine intervals yielded a stress profile across an immature fault zone intersecting the borehole, whereas the two intervals inside the fault zone could not be inverted because the injection pressures were too low to estimate the fracture normal stress.

The inversion does not yield a unique solution, but a set of admissible stress tensors that reproduce the measured activation vector within a misfit of 5° and satisfy the constraints on the fracture normal stress and vertical stress. We use the Euclidean mean of these tensors as the representative stress state of each interval. Not all principal stresses are equally well constrained. The least principal stress (S_3) is well resolved, with its orientation varying by a median of 8°–15° and its magnitude by an interquartile range of 3.1–5.8 MPa. In contrast, S_1 and S_2 can rotate and interchange within a common plane, so that the admissible solutions of each interval include both normal and strike-slip faulting stress states.

Over the whole stress profile, the Euclidean-mean stress tensors indicate a normal faulting regime ($A_\phi = 0.54$–0.86) with S_3 magnitudes of 8.5–15.1 MPa, with three intervals lying close to the transition to transtension. The derived S_{Hmax} magnitudes of 22.7–28.6 MPa agree well with previous mini-frac tests at the BedrettoLab, whereas S_{hmin} is lower in several intervals. The greatest principal stress (S_1) is inclined by 15°–37° from the vertical. Our study has revealed a counterclockwise rotation of S_3 by up to 68° (52° on average) adjacent to the MC fault zone relative to the far-field orientation of N22°E, which clearly exceeds the dispersion of the admissible solutions. In contrast, stress magnitudes vary little along the borehole. The rotation is asymmetric: it decays within 4–8 m above the fault zone but persists

over 17–23 m below it, in agreement with the wider zone of fractured rock below the fault core in a compound structure with multiple patches and relay zones. Slip on fault patches and, to a lesser degree, the compliance contrast between the fault damage zone and the host rock are hypothesized to be the primary contributors to this perturbation.

Hydraulic fractures showed measurable shear displacement and can be used as inversion input, but they are unfavorably oriented for slip and yield a larger dispersion of the admissible S_3 orientations than reactivated pre-existing fractures, whose results we therefore consider more robust. Additional limitations are that the discrete spacing of the test intervals only brackets rather than resolves the spatial extent of the stress perturbation, and that uncertainties in the input parameters (vertical stress, fracture normal stress, and fracture orientation) were not propagated into the inversion. Future work should incorporate these uncertainties directly into the inversion and better constrain the stress state within the fault zone itself, where the high permeability prevented reliable estimates of the fracture normal stress. Nonetheless, our results show that stress perturbations around even an immature fault zone can extend up to about 23 m into the host rock and primarily affect stress orientation rather than stress magnitude. Such local perturbations may be important for predicting hydraulic fracture propagation and the fault reactivation potential during hydraulic stimulations. SIMFIP-based stress inversion provides a means to resolve these perturbations at the meter scale and to estimate the complete stress tensor along a borehole profile.

Declarations

Acknowledgments

The SPINE project benefits from an exploration subsidy (contract number MF-021-GEO-ERK) from the Swiss Federal Office of Energy for the EGS geothermal project in Haute-Sorne, canton of Jura, which is gratefully acknowledged. We thank Barnabás Kövér for his valuable input and insightful discussions on the mini-frac tests conducted in the Earthquake Physics testbed at the BedrettoLab.

Availability of data and materials

The datasets used and analyzed during the current study are available from the corresponding author on reasonable request.

Competing interests

The authors declare that they have no competing interests.

Funding

This work was supported by the GEOTHERMICA SPINE project, with funding from the U.S. Department of Energy, Office of Energy Efficiency and Renewable Energy (AOP Task 1.1.7.10) and from the Swiss Federal Office of Energy (BFE, grant no. 200313-40011).

Authors' contributions

K.B. performed the stress inversion and data analysis, prepared the figures and tables, and wrote the manuscript. Y.G., F.S., P.C., and M.H. conducted the field experiments at the BedrettoLab, with the support of K.B. and B.V. F.S. processed the SIMFIP measurements and provided input data for the stress inversion. B.V. supervised the work, contributed to the interpretation of the results, and contributed to the manuscript text and figures. Y.G. contributed to the interpretation of the results and reviewed the manuscript. All authors read and approved the final manuscript.

A Logging and borehole trajectory

Two acoustic televiewer (ATV) logging runs were acquired in borehole BFE_A_05, before and after the SIMFIP injection experiments, on 29 November and 9 December 2022, to measured depths of 90.1 and 85.3 m, respectively. Only the upper half of the borehole was logged, as no test intervals are located at greater depths. Both runs were acquired with an ALT QL40-ABI-2G acoustic televiewer, which records its orientation with a three-axis fluxgate magnetometer and three accelerometers, from which the borehole azimuth and dip are derived. The azimuths of both runs were corrected for a magnetic declination of 2.5°.

As a reference, we use the three-dimensional trajectory of BFE_A_05 derived by Shakas et al. (2026) (trajectory version 2) for the boreholes of the Earthquake Physics testbed. In their processing pipeline, azimuth and dip from multiple wireline logging runs are corrected for magnetic declination, magnetic bias and sensor misalignment using an independent high-precision survey acquired with a prism and total-station system. Fig. A.1 compares the azimuth and dip of the two ATV runs with the reference

trajectory. Below the section affected by the conductor pipe, both logging runs match the reference trajectory relatively well. Down to 90 m MD, the reference trajectory has a mean azimuth of N30.9°E and a mean dip of 30.2°, i.e., the borehole plunges approximately towards the northeast.

The reference trajectory was used to compute the true vertical depths of the test intervals, required for the vertical stress estimation (Appendix B), and their spatial positions (Fig. 1c). In contrast, the orientations of the fractures picked from the ATV images were computed using the tool orientation recorded during the respective logging run, because the image and the orientation data are acquired simultaneously by the same probe.

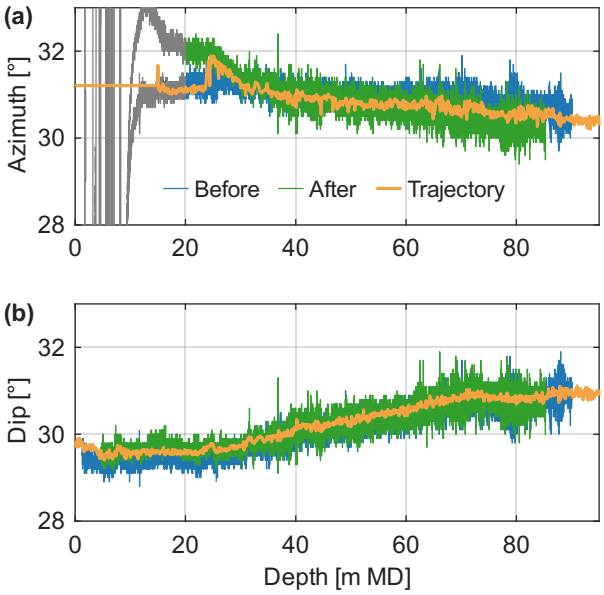


Figure A.1: Azimuth (a) and dip (b) of the ATV logs acquired before and after the SIMFIP experiments in borehole BFE_A_05, compared with the reference trajectory of Shakas et al. (2026), derived from multiple wireline logging runs combined with a total-station survey. All azimuths are corrected for a magnetic declination of 2.5°. ATV azimuths in the uppermost 20 m (gray) are affected by the metallic conductor pipe at the borehole collar.

B Vertical stress calculation

The vertical stress (S_v) at each interval depth was estimated by integrating the overburden density. The overburden at the location of borehole BFE_A_05 consists of approximately 1135 m of Rotondo granite, resulting in an overburden stress of about 29.2 MPa at the borehole collar, assuming a granite density of 2620 kg/m^3 (David et al., 2020). The vertical stress at depth was calculated using

$$S_v = \rho g(H_0 + \mathrm{TVD}), \tag{7}$$

where ρ is the rock density, g is gravitational acceleration, $H_0 = 1135$ m is the overburden at the borehole collar, and TVD is the true vertical depth of the test interval below the borehole collar.

C Fracture normal stress estimation

The fracture normal stress (S_n) was estimated from the jacking pressure determined by pressure–flow rate analysis (for methodological details, see Bröker and Ma 2022). We fitted one or two linear regressions to the data points on a pressure versus flow rate (P–Q) plot (e.g., Doe and Korbin, 1987; Rutqvist and Stephansson, 1996), where a bilinear trend indicates flow into the rock matrix at low pressures and into the open fracture once the pressure exceeds the jacking pressure. The jacking pressure is determined as the intersection of the two regression lines, or, if only one regression can be fitted, by backward extrapolation of the regression to a flow rate of $Q = 0$ L/min. In the latter case, the fracture is interpreted to have reopened during the initial pressurization step, as even low flow rates produce sufficiently high pressures in the low-permeability granite to cause fracture opening. The bilinear intersection was used for intervals 1, 2, 3, and 11, and the zero-flow intercept for intervals 4, 6, 9, and 10. If two regressions were fitted to the data of different cycles, the jacking pressures obtained from both were averaged. This applies to intervals 1 and 2 (bilinear intersection) and interval 6 (zero-flow intercept).

For intervals exhibiting a clear breakdown signature, such as interval 1 (Fig. 3a), only the data points recorded after breakdown were included in the open-fracture regression, because the fracture is assumed to be fully open at this stage, whereas data prior to breakdown reflect residual cohesion and incomplete fracture opening. In interval 11, we interpret the breakdown of the hydraulic fracture to have occurred during the step-rate test of cycle 2. A regression through the cycle 2 data yields a jacking pressure of 22.1 MPa, whereas the regression through the subsequent cycles 5–7 yields 17.9 MPa (Fig. A.2). Consistent with the procedure applied to the other intervals, only the post-breakdown cycles 5–7 were used to estimate the fracture normal stress. Because low flow rates were applied only during cycles 1 and 2, the matrix-flow regression of this interval is necessarily based on these cycles.

Interval 5 represents an exception. The interval pressures during injection were anomalously high, likely because the hydraulic fracture was initiated behind the upper packer. The resulting jacking pressures of 19.9 and 22.9 MPa (average 21.4 MPa) are the highest of all intervals and exceed the jacking pressures used for the other intervals, which range from 10.1 to 17.9 MPa. The regressions shown for this interval in Fig. A.2 were therefore not used. Instead, the fracture normal stress was taken as the average of the instantaneous shut-in pressures (ISIPs; see Bröker and Ma 2022 for details) of all analyzed cycles, determined using the inflection-point method of Gronseth and Kry (1981); Gronseth (1982). The resulting value of 16.3 MPa is consistent with the rebound of the upper packer pressure (14.1–16.0 MPa)

observed during shut-in, which we attribute to fracture closure. For intervals 7 and 8, located within the MC fault zone, no fracture normal stress could be estimated because injection pressures remained below 9 MPa due to the high permeability of the intervals. Consequently, these intervals were excluded from the stress inversion.

Fig. A.2 shows the P–Q plots of all analyzed intervals. The pressures shown are uphole values; the fracture normal stresses listed in Table 3 were obtained by adding the hydrostatic pressure of the fluid column between the pressure sensor in the tunnel and the interval depth.

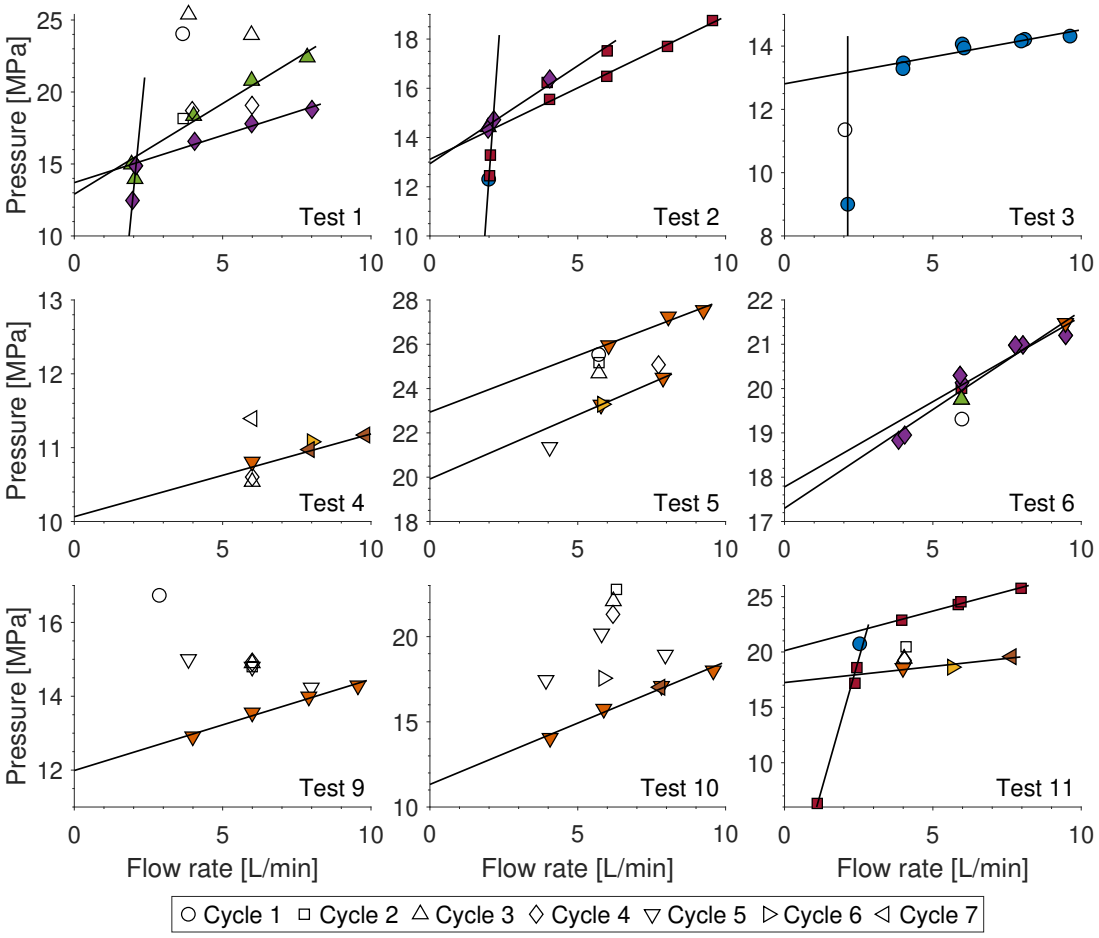


Figure A.2: P–Q analysis of the nine test intervals. Only the filled symbols are included in the calculation of the linear regressions. The jacking pressure was estimated from the intersection of the regressions or the zero-flow rate intersection. The pressure points shown are uphole values and are not corrected for hydrostatic pressure.

Supporting Information: Injection protocols and P–Q picks

Figs. A.3, A.4, and A.5 show the injection protocols of the nine test intervals analyzed in the paper. Gray shaded boxes show the injection cycles that were analyzed in the pressure transient analysis. Short injections with low flow rates (and thus low interval pressures), as well as cycles before breakdown in

intervals where a hydraulic fracture was created, were not analyzed. The picked pressure–flow rate points (P–Q points) are marked. All pressures shown in this section are uphole values recorded in the tunnel and are not corrected for the hydrostatic pressure of the fluid column in the injection line, whereas the fracture normal stresses reported in the main text include this correction.

- Interval 1: A leak in the injection line was discovered and fixed after cycle 1. The SIMFIP probe was unclamped between the two step-rate tests. The decreasing pressures with increasing flow rates during the two step-rate cycles indicate fracture propagation during the test. The jacking pressures of 15.6 and 15.1 MPa were estimated from the bilinear intersection separately for the two step-rate cycles, each using the step-down and the first step-up points, and were averaged.

- Interval 2: The shut-in curves of all cycles are very similar and the pressures at a given flow rate do not decrease between cycles, giving no indication of fracture propagation during the test. Two open-fracture regressions were fitted to the data of different cycles, giving jacking pressures of 14.3 and 14.6 MPa from the bilinear intersection, which were averaged.

- Interval 3: The optical fiber failed during the test, which had to be terminated early, so fewer injection cycles are available than in the other intervals. The breakdown pressure of 14.3 MPa is the lowest of all tests. Only one P–Q point lies below the jacking pressure, so the matrix-flow regression and thus the intersection of the two regressions (13.2 MPa) is poorly constrained. Backward extrapolation of the open-fracture regression gives a comparable value of 12.8 MPa. The pressure decline during the last flow rate step suggests that the fracture may have closed already before shut-in.

- Interval 4: The ISIP and G-function closure pressure, estimated from plots of dP/dG, match the fracture normal stress estimated by the jacking pressure on P–Q plots.

- Interval 5: The high interval pressures and breakdown pressure are likely caused by the initiation of a hydraulic fracture behind the upper packer. After shut-in, the interval pressure drops very quickly to pre-test values. At the same time, the upper packer pressure, which strongly increased during injection due to the rising interval pressure, shows a pronounced rebound at 14.1–16.0 MPa during cycles 2–6, which could be linked to the closure of the fracture. The P–Q jacking pressures were not used, and the fracture normal stress was estimated from the average ISIP instead (Appendix C).

- Interval 6: The high breakdown pressure implies that a hydraulic fracture was initiated in the interval. Two regressions were fitted depending on whether the points around 4 L/min are included, giving nearly identical zero-flow intercepts of 17.8 and 17.3 MPa, which were averaged.

- Interval 9: The decreasing pressures with increasing flow rates during the step-rate cycle indicate fracture propagation during the test.

- Interval 10: The high breakdown pressure shows that a hydraulic fracture was initiated in the interval. The decreasing pressures with increasing flow rates during the step-rate cycle indicate fracture propagation during the test. After shut-in, the interval pressure drops very quickly to pre-test values.

- Interval 11: The breakdown pressure is not given by a sharp peak, but its high value implies that a hydraulic fracture was initiated behind the upper packer during the step-rate test of cycle 2. After shut-in, the interval pressure drops very quickly to pre-test values. The jacking pressure derived from cycle 2 (22.1 MPa) is higher than that derived from the post-breakdown cycles 5–7 (17.9 MPa), as cycle 2 includes fracture initiation. Only the latter was used to estimate the fracture normal stress (Appendix C).

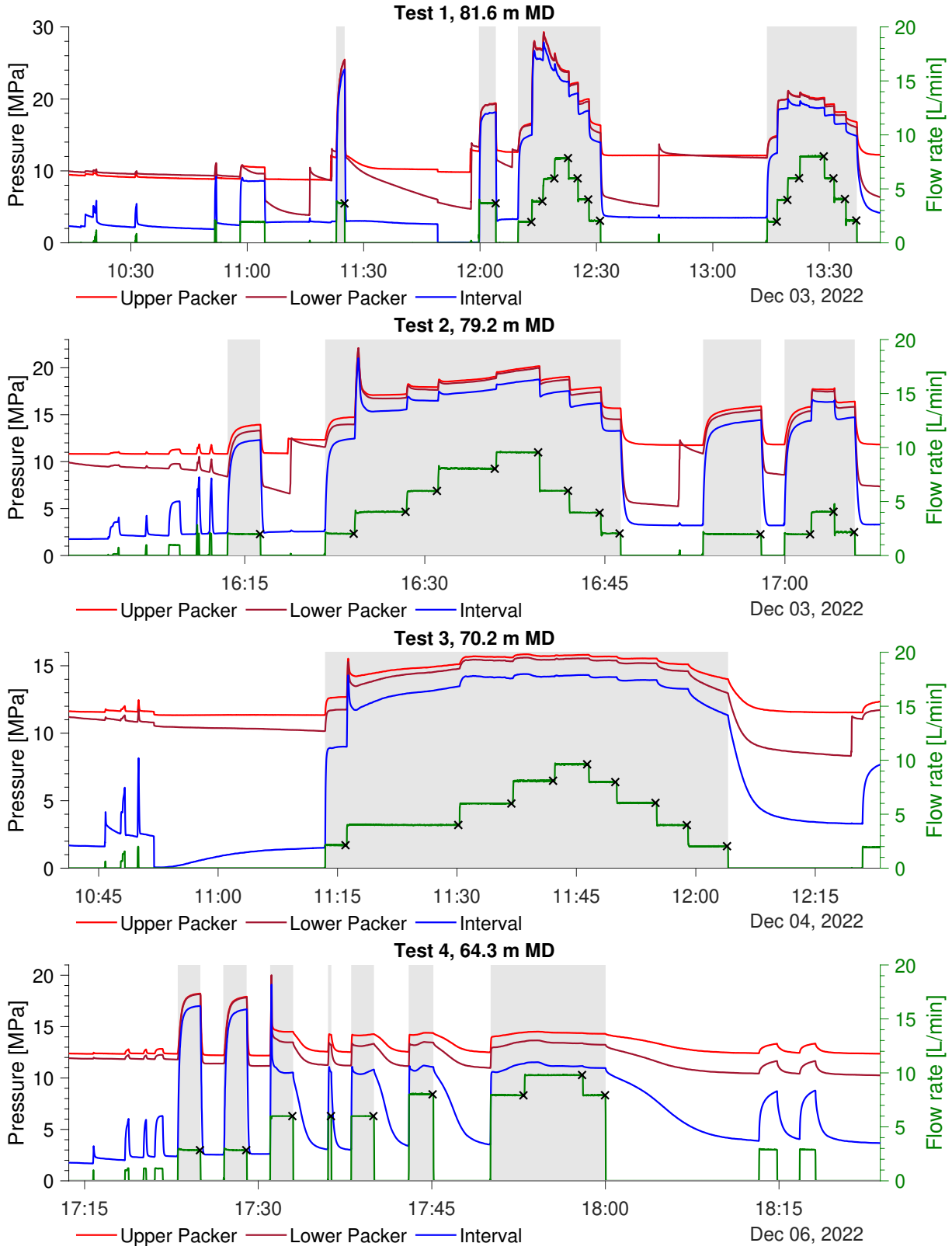


Figure A.3: Injection protocols for test intervals 1 to 4. All pressures are measured in the tunnel (uphole). Gray shaded periods show the injection cycles analyzed in the pressure transient analysis, while black X symbols mark the picked pressure–flow-rate (P–Q) points.

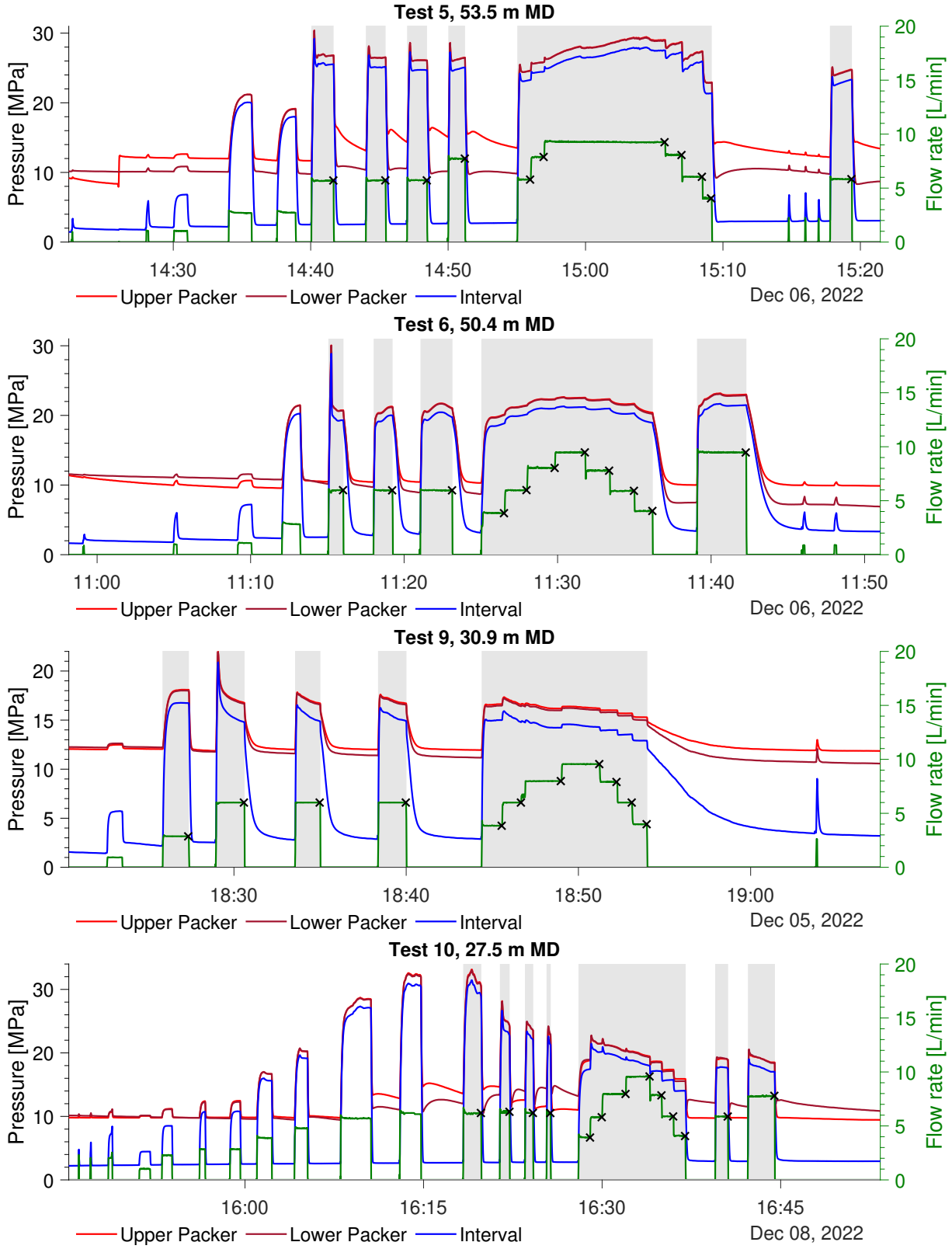


Figure A.4: Injection protocols for test intervals 5 to 10. Intervals 7 and 8 are not shown due to the very low pressures reached during injection into the major fault zone. All pressures are measured in the tunnel (uphole). Gray shaded periods show the injection cycles analyzed in the pressure transient analysis, while black X symbols mark the picked pressure–flow-rate (P–Q) points.

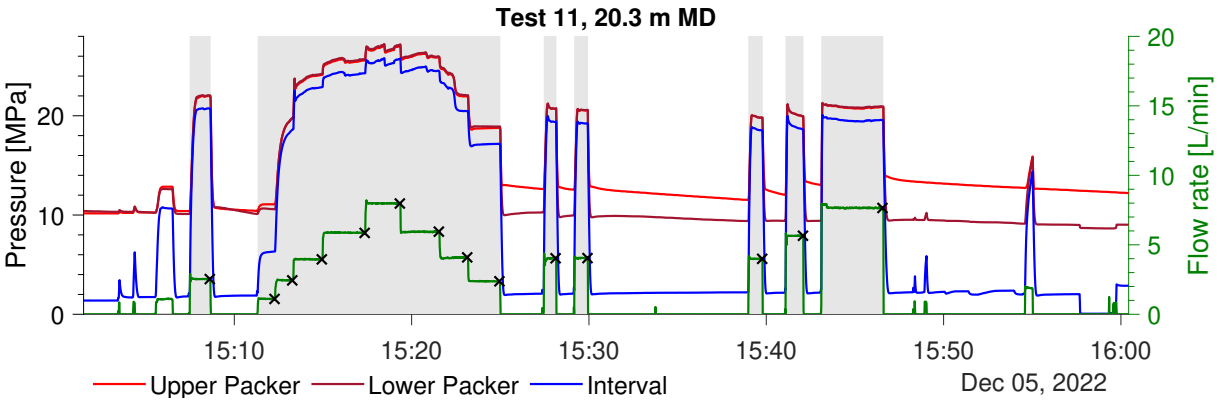


Figure A.5: Injection protocol for test interval 11. All pressures are measured in the tunnel (uphole). Gray shaded periods show the injection cycles analyzed in the pressure transient analysis, while black X symbols mark the picked pressure–flow-rate (P–Q) points.

References

Peter Achtziger-Zupančič, Alberto Ceccato, Alba Simona Zappone, Giacomo Pozzi, Alexis Shakas, Florian Amann, Whitney Maria Behr, Daniel Escallon Botero, Domenico Giardini, Marian Hertrich, Mohammadreza Jalali, Xiaodong Ma, Men-Andrin Meier, Julian Osten, Stefan Wiemer, and Massimo Cocco. Selection and characterization of the target fault for fluid-induced activation and earthquake rupture experiments. *Solid Earth*, 15:1087–1112, 8 2024. ISSN 1869-9529. doi: 10.5194/SE-15-1087-2024. URL https://se.copernicus.org/articles/15/1087/2024/.

Bernard Amadei and Ove Stephansson. *Rock Stress and Its Measurement*. Springer Netherlands, 1997. ISBN 978-94-010-6247-3. doi: 10.1007/978-94-011-5346-1. URL http://link.springer.com/10.1007/978-94-011-5346-1.

Ernest M Anderson. *The Dynamics of Faulting and Dyke Formation with Applications to Britain*. Oliver and Boyd, 2 edition, 1951.

Jacques Angelier. Determination of the mean principal directions of stresses for a given fault population. *Tectonophysics*, 56:T17–T26, 7 1979. ISSN 00401951. doi: 10.1016/0040-1951(79)90081-7.

Colleen A. Barton and Mark D. Zoback. Stress perturbations associated with active faults penetrated by boreholes: Possible evidence for near-complete stress drop and a new technique for stress magnitude measurement. *Journal of Geophysical Research: Solid Earth*, 99:9373–9390, 5 1994. ISSN 0148-0227. doi: 10.1029/93JB03359. URL https://agupubs.onlinelibrary.wiley.com/doi/10.1029/93JB03359.

M. H.P. Bott. The mechanics of oblique slip faulting. *Geological Magazine*, 96:109–117, 1959. ISSN 14695081. doi: 10.1017/S0016756800059987.

M. Brudy, M. D. Zoback, K. Fuchs, F. Rummel, and J. Baumgärtner. Estimation of the complete stress tensor to 8 km depth in the ktb scientific drill holes: Implications for crustal strength. *Journal of Geophysical Research: Solid Earth*, 102:18453–18475, 8 1997. ISSN 2156-2202. doi: 10.1029/96JB02942.

Kai Bröker and Xiaodong Ma. Estimating the least principal stress in a granitic rock mass: Systematic mini-frac tests and elaborated pressure transient analysis. *Rock Mechanics and Rock Engineering*, 55:1931–1954, 4 2022. ISSN 0723-2632. doi: 10.1007/s00603-021-02743-1. URL https://link.springer.com/10.1007/s00603-021-02743-1.

Kai Bröker, Xiaodong Ma, Shihuai Zhang, Nima Gholizadeh Doonechaly, Marian Hertrich, Gerd Klee, Andrew Greenwood, Eva Caspari, and Domenico Giardini. Constraining the stress field and its variability at the bedrettolab: Elaborated hydraulic fracture trace analysis. *International Journal of Rock Me-*

chanics and Mining Sciences, 178:105739, 6 2024. ISSN 13651609. doi: 10.1016/j.ijrmms.2024.105739. URL https://linkinghub.elsevier.com/retrieve/pii/S1365160924001047.

Kai Bröker, Benoît Valley, Florian Soom, Paul Cook, Yves Guglielmi, and Marian Hertrich. Stress field characterisation from fracture slip inversion at the bedrettolab. In *European Geothermal Congress 2025, 6-10 October*, 10 2025.

Kai Bröker, Yves Guglielmi, Florian Soom, Paul Cook, Marian Hertrich, and Benoît Valley. In situ quantification of fracture slip induced by hydraulic injections in a deep borehole: A comparison of two different borehole techniques. *International Journal of Rock Mechanics and Mining Sciences*, 202: 106516, 6 2026. ISSN 13651609. doi: 10.1016/j.ijrmms.2026.106516. URL https://linkinghub.elsevier.com/retrieve/pii/S1365160926001218.

Jonathan Saul Caine, James P. Evans, and Craig B. Forster. Fault zone architecture and permeability structure. *Geology*, 24:1025, 1996. ISSN 0091-7613. doi: 10.1130/0091-7613(1996)024⟨1025:FZAAPS⟩2.3.CO;2. URL https://pubs.geoscienceworld.org/geology/article/24/11/1025-1028/187969.

Frédéric Cappa, Yves Guglielmi, Christophe Nussbaum, Louis De Barros, and Jens Birkholzer. Fluid migration in low-permeability faults driven by decoupling of fault slip and opening. *Nature Geoscience*, 15:747–751, 9 2022. ISSN 1752-0894. doi: 10.1038/s41561-022-00993-4. URL https://www.nature.com/articles/s41561-022-00993-4.

A. Ceccato, W. M. Behr, A. S. Zappone, L. Tavazzani, and A. Giuliani. Structural evolution, exhumation rates, and rheology of the european crust during alpine collision: Constraints from the rotondo granite—gotthard nappe. *Tectonics*, 43:e2023TC008219, 6 2024. ISSN 1944-9194. doi: 10.1029/2023TC008219. URL https://onlinelibrary.wiley.com/doi/full/10.1029/2023TC008219https://onlinelibrary.wiley.com/doi/abs/10.1029/2023TC008219https://agupubs.onlinelibrary.wiley.com/doi/10.1029/2023TC008219.

Chandong Chang and Yeonguk Jo. Heterogeneous in situ stress magnitudes due to the presence of weak natural discontinuities in granitic rocks. *Tectonophysics*, 664:83–97, 11 2015. ISSN 00401951. doi: 10.1016/j.tecto.2015.08.044. URL https://linkinghub.elsevier.com/retrieve/pii/S0040195115004795.

Jin Hyuck Choi, Paul Edwards, Kyoungtae Ko, and Young Seog Kim. Definition and classification of fault damage zones: A review and a new methodological approach. *Earth-Science Reviews*, 152:70–87, 1 2016. ISSN 0012-8252. doi: 10.1016/J.EARSCIREV.2015.11.006.

C. David, M. Nejati, and D. Geremia. On petrophysical and geomechanical properties of bedretto granite. Technical report, ETH Zurich, 2020. URL http://hdl.handle.net/20.500.11850/428267.

Amy Day-Lewis, Mark Zoback, and Stephen Hickman. Scale-invariant stress orientations and seismicity rates near the san andreas fault. *Geophysical Research Letters*, 37:n/a–n/a, 12 2010. ISSN 00948276. doi: 10.1029/2010GL045025. URL http://doi.wiley.com/10.1029/2010GL045025.

T. W. Doe and G. E. Korbin. A comparison of hydraulic fracturing and hydraulic jacking stress measurements. In *28th U.S. Symposium on Rock Mechanics, USRMS 1987*, pages 283–290. American Rock Mechanics Association, 12 1987. doi: 10.1016/0148-9062(88)91180-1. URL https://linkinghub.elsevier.com/retrieve/pii/0148906288911801.

Nima Gholizadeh Doonechaly, Kai Bröker, Marian Hertrich, Martina Rosskopf, Anne Obermann, Virginie Durand, Francisco Serbeto, Alexis Shakas, Xiaodong Ma, Antonio Pio Rinaldi, Victor Clasen Repollés, Linus Villiger, Men-Andrin Meier, Valentin Gischig, Katrin Plenkers, Hansruedi Maurer, Stefan Wiemer, and Domenico Giardini. Insights from subsurface monitoring for engineering of the stimulation pattern in fractured reservoirs. *Rock Mechanics and Rock Engineering*, 58:8973–9000, 8 2025. ISSN 0723-2632. doi: 10.1007/s00603-025-04525-5. URL https://link.springer.com/10.1007/s00603-025-04525-5.

Laure Duboeuf, Louis De Barros, Maria Kakurina, Yves Guglielmi, Frederic Cappa, and Benoit Valley. Aseismic deformations perturb the stress state and trigger induced seismicity during injection experiments. *Geophysical Journal International*, 224:1464–1475, 1 2021. ISSN 0956-540X. doi: 10.1093/GJI/GGAA515. URL https://dx.doi.org/10.1093/gji/ggaa515.

D. R. Faulkner, T. M. Mitchell, D. Healy, and M. J. Heap. Slip on 'weak' faults by the rotation of regional stress in the fracture damage zone. *Nature*, 444:922–925, 12 2006. ISSN 0028-0836. doi: 10.1038/nature05353. URL https://www.nature.com/articles/nature05353.

Ke Gao and John P. Harrison. Re-examination of the in situ stress measurements on the 240 level of the aecl's url using tensor-based approaches. *Rock Mechanics and Rock Engineering*, 51:3179–3188, 10 2018. ISSN 0723-2632. doi: 10.1007/s00603-018-1530-1. URL http://link.springer.com/10.1007/s00603-018-1530-1.

Ke Gao and John P. Harrison. Examination of mean stress calculation approaches in rock mechanics. *Rock Mechanics and Rock Engineering*, 52:83–95, 1 2019. ISSN 0723-2632. doi: 10.1007/s00603-018-1568-0. URL http://link.springer.com/10.1007/s00603-018-1568-0.

J M Gronseth and P R Kry. Instantaneous shut-in pressure and its relationship to the minimum in situ stress. In *Workshop on Hydraulic Fracture Stress Measurements, Monterey, California*, pages 147–166, 1981.

J. Mark Gronseth. Determination of the instantaneous shut in pressure from hydraulic fracturing data and its reliability as a measure of the minimum principal stress. In *23rd U.S Symposium on Rock*

Mechanics (USRMS), Berkeley, California, August 1982. American Rock Mechanics Association, 6 1982. doi: 10.1016/0148-9062(83)91564-4. URL https://linkinghub.elsevier.com/retrieve/pii/0148906283915644.

Y. Guglielmi, P. Cook, F. Soom, M. Schoenball, P. Dobson, and T. Kneafsey. In situ continuous monitoring of borehole displacements induced by stimulated hydrofracture growth. *Geophysical Research Letters*, 48:e2020GL090782, 2 2021a. ISSN 0094-8276. doi: 10.1029/2020GL090782. URL https://agupubs.onlinelibrary.wiley.com/doi/10.1029/2020GL090782.

Yves Guglielmi, Frederic Cappa, Hervé Lançon, Jean Bernard Janowczyk, Jonny Rutqvist, C. F. Tsang, and J. S. Y. Wang. Isrm suggested method for step-rate injection method for fracture in-situ properties (simfip): Using a 3-components borehole deformation sensor. *Rock Mechanics and Rock Engineering*, 47:303–311, 1 2014. ISSN 0723-2632. doi: 10.1007/s00603-013-0517-1.

Yves Guglielmi, Kazuhiro Aoki, Paul Cook, Florian Soom, Frédéric Cappa, and Yukumo Tanaka. Characterizing the reactivation mechanisms of coseismic surface ruptures associated with the 2011 mw 6.7 fukushima-ken hamadori earthquake in japan through borehole hydromechanical testing. *Tectonophysics*, 819:229084, 11 2021b. ISSN 0040-1951. doi: 10.1016/J.TECTO.2021.229084.

Yves Guglielmi, Mark McClure, Jeffrey Burghardt, Joseph P. Morris, Thomas Doe, Pengcheng Fu, Hunter Knox, Vince Vermeul, Tim Kneafsey, J. Ajo-Franklin, T. Baumgartner, K. Beckers, D. Blankenship, A. Bonneville, L. Boyd, S. Brown, J.A. Burghardt, C. Chai, A. Chakravarty, T. Chen, Y. Chen, B. Chi, K. Condon, P.J. Cook, D. Crandall, P.F. Dobson, T. Doe, C.A. Doughty, D. Elsworth, J. Feldman, Z. Feng, A. Foris, L.P. Frash, Z. Frone, P. Fu, K. Gao, A. Ghassemi, Y. Guglielmi, B. Haimson, A. Hawkins, J. Heise, C. Hopp, M. Horn, R.N. Horne, J. Horner, M. Hu, H. Huang, L. Huang, K.J. Im, M. Ingraham, E. Jafarov, R.S. Jayne, T.C. Johnson, S.E. Johnson, B. Johnston, S. Karra, K. Kim, D.K. King, T. Kneafsey, H. Knox, J. Knox, D. Kumar, K. Kutun, M. Lee, D. Li, J. Li, K. Li, Z. Li, M. Maceira, P. Mackey, N. Makedonska, C.J. Marone, E. Mattson, M.W. McClure, J. McLennan, T. McLing, C. Medler, R.J. Mellors, E. Metcalfe, J. Miskimins, J. Moore, C.E. Morency, J.P. Morris, T. Myers, S. Nakagawa, G. Neupane, G. Newman, A. Nieto, T. Paronish, R. Pawar, P. Petrov, B. Pietzyk, R. Podgorney, Y. Polsky, J. Pope, S. Porse, J.C. Primo, T. Pyatina, C. Reimers, B.Q. Roberts, M. Robertson, V. Rodríguez-Tribaldos, W. Roggenthen, J. Rutqvist, D. Rynders, M. Schoenball, P. Schwering, V. Sesetty, C.S. Sherman, A. Singh, M.M. Smith, H. Sone, E.L. Sonnenthal, F.A. Soom, D.P. Sprinkle, S. Sprinkle, C.E. Strickland, J. Su, D. Templeton, J.N. Thomle, C. Ulrich, N. Uzunlar, A. Vachaparampil, C.A. Valladao, W. Vandermeer, G. Vandine, D. Vardiman, V.R. Vermeul, J.L. Wagoner, H.F. Wang, J. Weers, N. Welch, J. White, M.D. White, P. Winterfeld, T. Wood, S. Workman, H. Wu, Y.S. Wu, E.C. Yildirim, Y. Zhang, Y.Q. Zhang, Q. Zhou, and M.D. Zoback. Using in-situ strain measurements to evaluate the accuracy of stress estima-

tion procedures from fracture injection/shut-in tests. *International Journal of Rock Mechanics and Mining Sciences*, 170:105521, 10 2023. ISSN 13651609. doi: 10.1016/j.ijrmms.2023.105521. URL https://linkinghub.elsevier.com/retrieve/pii/S1365160923001958.

Yves Guglielmi, Auli Niemi, Chin Fu Tsang, Patrick Dobson, Paul Cook, Christopher Juhlin, Benoît Dessirier, Alexandru Tatomir, Farzad Basirat, Henning Lorenz, Jan Erik Rosberg, Emil Lundberg, Bjarne Almqvist, and Roland Roberts. A field test on the hydromechanical behaviour of flowing and nonflowing fractures in the 2.5 km cosc-1 borehole in crystalline rock, sweden. *Hydrogeology Journal*, 33:425–448, 3 2025. ISSN 14350157. doi: 10.1007/s10040-025-02886-3. URL https://link.springer.com/article/10.1007/s10040-025-02886-3.

B.C. C. Haimson and F.H. H. Cornet. Isrm suggested methods for rock stress estimation-part 3: Hydraulic fracturing (hf) and/or hydraulic testing of pre-existing fractures (htpf). *International Journal of Rock Mechanics and Mining Sciences*, 40:1011–1020, 10 2003. ISSN 13651609. doi: 10.1016/j.ijrmms.2003.08.002. URL https://linkinghub.elsevier.com/retrieve/pii/S1365160903001254.

Pooya Hamdi, Simon Ufrecht, Peter Achtziger-Zupančič, Kai Bröker, Xiaodong Ma, and Florian Amann. Understanding the regional stress in active tectonic regime using 3d numerical modeling, case study of bedrettolab, switzerland. *Rock Mechanics and Rock Engineering*, 58:12187–12206, 11 2025. ISSN 0723-2632. doi: 10.1007/s00603-025-04740-0. URL https://link.springer.com/10.1007/s00603-025-04740-0.

David Healy. Damage patterns, stress rotations and pore fluid pressures in strike-slip fault zones. *Journal of Geophysical Research: Solid Earth*, 113:12407, 12 2008. ISSN 0148-0227. doi: 10.1029/2008JB005655. URL https://agupubs.onlinelibrary.wiley.com/doi/10.1029/2008JB005655.

Maria Kakurina. *Mechanics of fault reactivation and its application to stress measurements*. PhD thesis, Université de Neuchâtel, 2019. URL https://libra.unine.ch/handle/123456789/29864.

Maria Kakurina, Yves Guglielmi, Christophe Nussbaum, and Benoît Valley. Slip perturbation during fault reactivation by a fluid injection. *Tectonophysics*, 757:140–152, 4 2019. ISSN 0040-1951. doi: 10.1016/J.TECTO.2019.01.017.

Maria Kakurina, Yves Guglielmi, Christophe Nussbaum, and Benoît Valley. In situ direct displacement information on fault reactivation during fluid injection. *Rock Mechanics and Rock Engineering*, 53:4313–4328, 10 2020. ISSN 0723-2632. doi: 10.1007/s00603-020-02160-w. URL https://link.springer.com/10.1007/s00603-020-02160-w.

W. Barclay Kamb. Ice petrofabric observations from blue glacier, washington, in relation to theory and experiment. *Journal of Geophysical Research*, 64:1891–1909, 11 1959. ISSN 2156-2202.

doi: 10.1029/JZ064I011P01891. URL https://onlinelibrary.wiley.com/doi/full/10.1029/JZ064i011p01891https://onlinelibrary.wiley.com/doi/abs/10.1029/JZ064i011p01891https://agupubs.onlinelibrary.wiley.com/doi/10.1029/JZ064i011p01891.

Young Seog Kim, David C.P. Peacock, and David J. Sanderson. Fault damage zones. *Journal of Structural Geology*, 26:503–517, 3 2004. ISSN 0191-8141. doi: 10.1016/J.JSG.2003.08.002.

Geoffrey C. P. King, Ross S. Stein, and Jian Lin. Static stress changes and the triggering of earthquakes. *Bulletin of the Seismological Society of America*, 84:935–953, 6 1994. ISSN 1943-3573. doi: 10.1785/BSSA0840030935. URL https://pubs.geoscienceworld.org/bssa/article/84/3/935/102745/Static-stress-changes-and-the-triggering-of.

Hannes Krietsch, Valentin Gischig, Keith Evans, Joseph Doetsch, Nathan Oliver Dutler, Benoît Valley, and Florian Amann. Stress measurements for an in situ stimulation experiment in crystalline rock: Integration of induced seismicity, stress relief and hydraulic methods. *Rock Mechanics and Rock Engineering*, 52:517–542, 2 2019. ISSN 07232632. doi: 10.1007/s00603-018-1597-8. URL http://link.springer.com/10.1007/s00603-018-1597-8.

Barnabás Kövér, Valentin Gischig, Jordan Aaron, Kai Bröker, Men-Andrin Meier, Marian Hertrich, Radhika de Silva, Alessandro Profeta, Domenico Giardini, and Stefan Wiemer. Characterization of stress heterogeneity around a fault zone based on inversion of hydraulic fracturing tests. Submitted to IJRMMS (preprint pending), 2026.

Bing Q. Li and Herbert H. Einstein. Direct and microseismic observations of hydraulic fracturing in barre granite and opalinus clayshale. *Journal of Geophysical Research: Solid Earth*, 124:11900–11916, 11 2019. ISSN 2169-9356. doi: 10.1029/2019JB018376. URL https://onlinelibrary.wiley.com/doi/full/10.1029/2019JB018376https://onlinelibrary.wiley.com/doi/abs/10.1029/2019JB018376https://agupubs.onlinelibrary.wiley.com/doi/10.1029/2019JB018376.

Weiren Lin, En-Chao Yeh, Jih-Hao Hung, Bezalel Haimson, and Tetsuro Hirono. Localized rotation of principal stress around faults and fractures determined from borehole breakouts in hole b of the taiwan chelungpu-fault drilling project (tcdp). *Tectonophysics*, 482:82–91, 2 2010. ISSN 00401951. doi: 10.1016/j.tecto.2009.06.020. URL https://linkinghub.elsevier.com/retrieve/pii/S0040195109003539.

C. Ljunggren, Yanting Chang, T. Janson, and R. Christiansson. An overview of rock stress measurement methods. *International Journal of Rock Mechanics and Mining Sciences*, 40:975–989, 10 2003. ISSN 13651609. doi: 10.1016/j.ijrmms.2003.07.003. URL https://linkinghub.elsevier.com/retrieve/pii/S1365160903001230.

Björn Lund and John Townend. Calculating horizontal stress orientations with full or partial knowledge of the tectonic stress tensor. *Geophysical Journal International*, 170:1328–1335, 9 2007. ISSN 0956540X. doi: 10.1111/j.1365-246X.2007.03468.x. URL https://academic.oup.com/gji/article-lookup/doi/10.1111/j.1365-246X.2007.03468.x.

Volker Lützenkirchen and Simon Loew. Late alpine brittle faulting in the rotondo granite (switzerland): deformation mechanisms and fault evolution. *Swiss Journal of Geosciences*, 104:54, 2011. doi: 10.1007/s00015-010-0050-0. URL http://hdl.handle.net/20.500.11850/36505.

Xiaodong Ma and Mark D. Zoback. Lithology-controlled stress variations and pad-scale faults: A case study of hydraulic fracturing in the woodford shale, oklahoma. *GEOPHYSICS*, 82:ID35–ID44, 11 2017. ISSN 0016-8033. doi: 10.1190/geo2017-0044.1.

Xiaodong Ma, Marian Hertrich, Florian Amann, Kai Bröker, Nima Gholizadeh Doonechaly, Valentin Gischig, Rebecca Hochreutener, Philipp Kästli, Hannes Krietsch, Michèle Marti, Barbara Nägeli, Morteza Nejati, Anne Obermann, Katrin Plenkers, Antonio P. Rinaldi, Alexis Shakas, Linus Villiger, Quinn Wenning, Alba Zappone, Falko Bethmann, Raymi Castilla, Francisco Seberto, Peter Meier, Thomas Driesner, Simon Loew, Hansruedi Maurer, Martin O. Saar, Stefan Wiemer, and Domenico Giardini. Multi-disciplinary characterizations of the bedrettolab – a new underground geoscience research facility. *Solid Earth*, 13:301–322, 2 2022a. ISSN 1869-9529. doi: 10.5194/se-13-301-2022. URL https://se.copernicus.org/articles/13/301/2022/.

Xiaodong Ma, Shihuai Zhang, Xiaowen Zhang, Jiandong Liu, Juan Jin, Wei Cheng, Weidong Jiang, Guangming Zhang, Zhaowei Chen, and Mark D. Zoback. Lithology-controlled stress variations of longmaxi shale – example of an appraisal wellbore in the changning area. *Rock Mechanics Bulletin*, 1:100002, 10 2022b. ISSN 27732304. doi: 10.1016/j.rockmb.2022.100002. URL https://linkinghub.elsevier.com/retrieve/pii/S2773230422000026.

Men-Andrin Meier, Paul Selvadurai, Valentin Gischig, Marian Hertrich, Elisa Tinti, Antonio Pio Rinaldi, Mohammedreza Jalali, Elena Spagnuolo, Alba Zappone, Luca Dal Zilio, Giacomo Pozzi, Frédérick Massin, Alberto Ceccato, Alexis Shakas, Peter Achtziger-Zupančič, Stefano Aretusini, Viola Becattini, Kathrin Behnen, Kai Bröker, Victor Clasen Repollés, John Clinton, Cristiano Collettini, Paul Cook, Chiara Cornelio, Georgia Cua, Nikolaj Dahmen, Jonas Dickmann, Fiona Dresler-Dorn, Virginie Durand, Pascal Edme, Nima Gholizadeh Doonechaly, Giuseppe Volpe, Yves Guglielmi, Ivo Graber, Thomas Haag, Leon Hibbard, Rebecca Hochreutener, Danyang Jiang, Philipp Kästli, Barnabas Kövér, Michal Kruszewski, Aurora Lambiase, Federica Lanza, Laura Laurenti, Alexandra Lightfoot, Cara Magnabosco, Michèle Marti, Hansruedi Maurer, Olivier Meyers, Leila Mizrahi, Francesco Mosconi, Anne Obermann, Kadek Palgunadi, Edoardo Pezzulli, Katrin Plenkers, Giulio Poggiali,

Pooya Hamdi, Martina Rosskopf, Luca Scarabello, Tom Schaber, Nico Schliwa, Ryan Schultz, Miriam Schwarz, Florian Soom, Mariano Supino, Lu Tian, Katinka Tuinstra, Liliana Vargas Meleza, Linus Villiger, Zhe Wang, Mathilde Wimez, Jiayi Ye, Stefanie Zeller, Eric Zimmermann, Florian Amann, Massimo Cocco, Stefan Wiemer, and Domenico Giardini. Activating a natural fault zone in the swiss alps. *Seismica*, 5, 2 2026. ISSN 2816-9387. doi: 10.26443/seismica.v5i1.2065. URL https://seismica.library.mcgill.ca/article/view/2065.

D. C.P. Peacock, V. Dimmen, A. Rotevatn, and D. J. Sanderson. A broader classification of damage zones. *Journal of Structural Geology*, 102:179–192, 9 2017. ISSN 0191-8141. doi: 10.1016/J.JSG.2017.08.004.

David D. Pollard and Paul Segall. *Theoretical displacements and stresses near fractures in rock: With applications to faults, joints, veins, dikes, and solution surfaces*, pages 277–349. Elsevier, 1 1987. doi: 10.1016/B978-0-12-066266-1.50013-2. URL https://linkinghub.elsevier.com/retrieve/pii/B9780120662661500132.

Markus Rast, Andrea Galli, Jonas B. Ruh, Marcel Guillong, and Claudio Madonna. Geology along the bedretto tunnel: kinematic and geochronological constraints on the evolution of the gotthard massif (central alps). *Swiss Journal of Geosciences*, 115:8, 12 2022. ISSN 1661-8726. doi: 10.1186/s00015-022-00409-w. URL https://link.springer.com/10.1186/s00015-022-00409-w.

Karsten Reiter. Stress rotation-impact and interaction of rock stiffness and faults. *Solid Earth*, 12: 1287–1307, 6 2021. ISSN 18699529. doi: 10.5194/SE-12-1287-2021.

J. Rutqvist and O. Stephansson. A cyclic hydraulic jacking test to determine the in situ stress normal to a fracture. *International Journal of Rock Mechanics and Mining Sciences and Geomechanics*, 33: 695–711, 10 1996. ISSN 01489062. doi: 10.1016/0148-9062(96)00013-7. URL https://linkinghub.elsevier.com/retrieve/pii/0148906296000137.

D.P. Sahara, M. Schoenball, T. Kohl, and B.I.R. Müller. Impact of fracture networks on borehole breakout heterogeneities in crystalline rock. *International Journal of Rock Mechanics and Mining Sciences*, 71:301–309, 10 2014. ISSN 13651609. doi: 10.1016/j.ijrmms.2014.07.001. URL https://linkinghub.elsevier.com/retrieve/pii/S136516091400166X.

Tom Schaber, Mohammedreza Jalali, Alberto Ceccato, Alba Simona Zappone, Giacomo Pozzi, Valentin Gischig, Marian Hertrich, Men-Andrin Meier, Timo Seemann, Hannes Claes, Yves Guglielmi, Domenico Giardini, Stefan Wiemer, Massimo Cocco, and Florian Amann. Multi-scale hydraulic and petrophysical characterization of a heterogeneous fault zone in the gotthard massif's crystalline basement. *Solid Earth*, 17:275–295, 2 2026. ISSN 1869-9510. doi: 10.5194/SE-17-275-2026. URL https://se.copernicus.org/articles/17/275/2026/.

Alexis Shakas, Marian Hertrich, Valentin Gischig, Domenico Giardini, Men-Andrin Meier, Mathilde Wimez, Liliana Vargas Meleza, Barnabas Kövér, Alba Simona Zappone, Pooya Hamdi, Patrick Pfammatter, Alberto Ceccato, and Leon Hibbard. Fear borehole trajectories: Bedretto lab fault activation and earthquake rupture project [data set], 3 2026. URL http://hdl.handle.net/20.500.11850/797493.

Gadi Shamir and Mark D. Zoback. Stress orientation profile to 3.5 km depth near the san andreas fault at cajon pass, california. *Journal of Geophysical Research*, 97:5059, 1992. ISSN 0148-0227. doi: 10.1029/91JB02959.

Robert W. Simpson. Quantifying anderson's fault types. *Journal of Geophysical Research: Solid Earth*, 102:17909–17919, 8 1997. ISSN 01480227. doi: 10.1029/97JB01274.

Florian Soom, Yves Guglielmi, Paul Cook, Kai Bröker, Benoît Valley, and Marian Hertrich. Spine report: Simfip probe field tests at bedretto lab, december 2022. Technical report, 10 2026. URL http://hdl.handle.net/20.500.11850/808220.

Mayukh Talukdar, Hiroki Sone, and Li-Wei Kuo. Lithology and fault-related stress variations along the tcdp boreholes: The stress state before and after the 1999 chi-chi earthquake. *Journal of Geophysical Research: Solid Earth*, 127:e2021JB023290, 2 2022. ISSN 2169-9313. doi: 10.1029/2021JB023290. URL https://agupubs.onlinelibrary.wiley.com/doi/10.1029/2021JB023290.

Benoît Valley and Keith F. Evans. Stress orientation to 5 km depth in the basement below basel (switzerland) from borehole failure analysis. *Swiss Journal of Geosciences*, 102:467, 12 2009. ISSN 1661-8726. doi: 10.1007/s00015-009-1335-z.

Benoît Valley and Keith F Evans. Stress heterogeneity in the granite of the soultz egs reservoir inferred from analysis of wellbore failure. In *Proceedings World Geothermal Congress*, pages 25–29, 2010.

Frederick W. Vollmer. C program for automatic contouring of spherical orientation data using a modified kamb method. *Computers & Geosciences*, 21:31–49, 2 1995. ISSN 0098-3004. doi: 10.1016/0098-3004(94)00058-3.

Robert E. Wallace. Geometry of shearing stress and relation to faulting. *The Journal of Geology*, 59: 118–130, 3 1951. ISSN 0022-1376. doi: 10.1086/625831.

Guangyu Wang, Xiaodong Ma, Shihuai Zhang, Kai Bröker, Marian Hertrich, and Domenico Giardini. Continuous spatial stress variations within a granitic rock mass: Revealed by cross-sectional ellipticity of an array of boreholes. *International Journal of Rock Mechanics and Mining Sciences*, 206:106627, 10 2026. ISSN 1365-1609. doi: 10.1016/J.IJRMMS.2026.106627. URL https://linkinghub.elsevier.com/retrieve/pii/S1365160926002327.

A. Yamaji. Are the solutions of stress inversion correct? visualization of their reliability and the separation of stresses from heterogeneous fault-slip data. *Journal of Structural Geology*, 25:241–252, 2 2003. ISSN 0191-8141. doi: 10.1016/S0191-8141(02)00021-4.

Arno Zang and Ove Stephansson. *Stress Field of the Earth's Crust*. Springer Netherlands, 2010. ISBN 978-1-4020-8443-0. doi: 10.1007/978-1-4020-8444-7. URL http://link.springer.com/10.1007/978-1-4020-8444-7.

Shihuai Zhang and Xiaodong Ma. How does in situ stress rotate within a fault zone? insights from explicit modeling of the frictional, fractured rock mass. *Journal of Geophysical Research: Solid Earth*, 126, 11 2021. ISSN 2169-9313. doi: 10.1029/2021JB022348. URL https://agupubs.onlinelibrary.wiley.com/doi/10.1029/2021JB022348.

Shihuai Zhang, Xiaodong Ma, Kai Bröker, Rutger van Limborgh, Quinn Wenning, Marian Hertrich, and Domenico Giardini. Fault zone spatial stress variations in a granitic rock mass: Revealed by breakouts within an array of boreholes. *Journal of Geophysical Research: Solid Earth*, 128, 8 2023. ISSN 2169-9313. doi: 10.1029/2023JB026477. URL https://agupubs.onlinelibrary.wiley.com/doi/10.1029/2023JB026477.

Moritz O Ziegler, Robin Seithel, Thomas Niederhuber, Oliver Heidbach, Thomas Kohl, Birgit Müller, Mojtaba Rajabi, Karsten Reiter, and Luisa Röckel. Stress state at faults: the influence of rock stiffness contrast, stress orientation, and ratio. *Solid Earth*, 15:1047–1063, 2024. doi: 10.5194/se-15-1047-2024. URL https://doi.org/10.5194/se-15-1047-2024.

M. L. Zoback. First-and second-order patterns of stress in the lithosphere: the world stress map project. *Journal of Geophysical Research*, 97, 1992. ISSN 01480227. doi: 10.1029/92JB00132.

Mark D. Zoback. *Reservoir Geomechanics*. Cambridge University Press, 2007. ISBN 9780511586477. doi: 10.1017/CBO9780511586477. URL http://ebooks.cambridge.org/ref/id/CBO9780511586477.